Assessment of power losses and structural response of offshore floating solar platform

Alcañiz, Alba; Agarwal, Shagun; Tiwald, Philipp; Isabella, Olindo; Ziar, Hesan; Colomés, Oriol

DOI
10.1016/j.energy.2025.137656

Publication date
2025

Document Version
Final published version

Published in
Energy

Energy 335 (2025) 137656

Contents lists available at ScienceDirect

Energy

journal homepage: www.elsevier.com/locate/energy

Assessment of power losses and structural response of offshore floating solar platform

Alba Alcañiz [a,*], Shagun Agarwal [b,*], Philipp Tiwald [a], Olindo Isabella [a], Hesan Ziar [a], Oriol Colomés [b]

[a] Faculty of Electrical Engineering, Mathematics and Computer Science, TU Delft, The Netherlands
[b] Faculty of Civil Engineering and Geosciences, TU Delft, The Netherlands

ARTICLE INFO

Keywords:
Floating photovoltaic
Finite element methods
Monolithic
Power mismatch losses
Hydroelasticity

ABSTRACT

As climate change becomes more critical and renewable energy sources expand, land-based photovoltaic (PV) systems face limitations due to competition with agriculture and housing. The sea offers a promising location for offshore floating PV (OFPV) systems. Understanding fluid–structure interactions is crucial for these systems. This work explores how different parameters affect the structural load on the floating platform and related electrical power losses. We develop a multi-physics framework integrating the mechanical model of a large floating structure with the optoelectrical modeling of PV modules. This framework analyzes a hypothetical OFPV platform design with various floater configurations, from a single large floater to multiple small floaters connected with free hinges. The results reveal a trade-off in the number of floaters. Power mismatch loss is lower for platforms with fewer, longer floaters. However, structural loads vary, with high stresses in longer floaters due to the elastic response. Young's modulus impacts longer floaters where the elastic response dominates, while cross-section fill ratio affects shorter floaters, where the rigid-body response prevails. The floater-beam thickness has the most significant impact across various floater lengths.

1. Introduction

Climate change is one of the most pressing global challenges and its consequences can be drastic if no immediate action is taken [1]. The urgency to transition to renewable energy sources has never been greater. Photovoltaic (PV) power plays a pivotal role in this energy transition, offering a sustainable and environmentally friendly solution to meet the growing energy demands. However, large-scale PV installations have significant land requirements, which can pressure sectors such as accommodation or agriculture [2]. Land scarcity is even more pronounced in densely populated areas near the coastline with high electricity demand [3].

Under this context, the sea presents a promising location for renewable energy installations. While offshore wind technology is well-established, with over 2,600 wind turbines installed in the North Sea [4], offshore floating photovoltaic (OFPV) systems are an emerging technology. This technology has an immense potential that could cover the energy needs of over 11 billion people if only the most favorable locations are employed [5].

A key factor to consider in OFPV installations is the inherent fluid–structure interaction (FSI), i.e., the interaction of the floating platform with ocean waves. This is particularly relevant for the truly offshore deployment of floating PV. The consequences of this FSI are twofold: (1) the FSI results in structural loads within the floaters and joints of the floating island, depending on both the configuration and properties of the floater and sea waves; (2) the FSI results in a dynamic change in the tilt of the individual PV panels, resulting in potential power losses due to power mismatch and movement [6]. Therefore, the hydroelastic response of OFPV platform has significant multi-physical structural and opto-electrical implications.

So far in the literature, the structural analysis of OFPV platforms has largely been done using simplified approaches, owing to the complexity of the problem. The structural deformation of OFPV platforms has been investigated using the Froude–Krylov method for estimating the wave force [7,8]. This basic method has several limitations, such as assuming undisturbed waves, disregarding diffraction, lack of hydrodynamic coefficients for thin-floating platforms, and inability to resolve the difference in loads between boundaries and inner regions of the floating PV platform. Alternative simplified methods involve estimating the rotational motion of a single rigid panel based on undisturbed wave energy density [9], however, their rudimentary assumptions restrict their applicability. Recent studies on hydro-elastic interaction between

* Corresponding authors.
E-mail addresses: A.AlcanizMoya@tudelft.nl (A. Alcañiz), S.Agarwal@tudelft.nl (S. Agarwal).

https://doi.org/10.1016/j.energy.2025.137656
Received 15 July 2024; Received in revised form 15 June 2025; Accepted 18 July 2025
Available online 5 August 2025

small amplitude linear waves and perforated elastic plates using the arbitrary Lagrangian–Eulerian methodology show limited accuracy for regular-wave tests compared to the corresponding experiments [10], thus highlighting the challenges in simulating OFPV structures. Wave and wind loads can exert significant pressure on the floating and mooring structure, resulting in loads in the order of mega-Newton as suggested by a quasi-static analytical model [11]. The stress experienced by the connection pins and the structural components is addressed by Sree et al. [10]. These studies contribute to a better understanding of the mechanical aspects and structural integrity of OFPV systems.

The literature currently lacks a thorough investigation into the effects of hydroelastic responses on power generation in OFPV systems. In [9], the performance of an OFPV system is compared with that of a land-based one by using a simplified representation of the sea. In a previous work [6], that study was extended to two dimensions but key assumptions remained, including that the wave field was unaffected by the floating structure, the wave force on the floating body was estimated using the Froude–Krylov approach, and the floating body was considered rigid. Additionally, power mismatch losses were not addressed in either of the manuscripts. The measurements conducted by Dörenkämper et al. address the mismatch issue in [12]. They reported power mismatch losses of 3%, 7%, and 9% for median wave heights of 0.1, 0.4, and 1.5 m, respectively. These losses differ from the measured ones in [13], where the mismatch losses were 1.6%, 2.4%, and 3.7% for average wave heights of 0.25, 0.5, and 1 m, respectively. These differences may stem from variations in floater characteristics. However, none of these studies tackle the origin of this disparity, making it challenging to identify the source of the discrepancies.

The preceding discussion therefore makes it evident that current literature lacks a comprehensive multi-physics analysis of floating photovoltaic (PV) platforms. While some studies address the mechanical response of floating pontoons, they generally fall into one of two categories, each with limitations. The first involves complex hydroelastic analyses of one or a few pontoons, which are not easily scalable to large platforms or long simulations of irregular sea-state. The second relies on highly simplified structural models that often neglect hydroelastic fluid–structure interactions.

Similarly, existing studies on the photovoltaic performance of floating PV systems tend to use overly simplified representations of structural interactions with waves and wave-induced loads. In offshore floating PV (OFPV) systems, structural response and photovoltaic performance are inherently interconnected. Oversimplifying either aspect can result in an incomplete or unreliable analysis.

This research aims to lay the groundwork for a comprehensive, multidisciplinary analysis of OFPV systems. Specifically, it accounts for the hydroelastic response of OFPV platforms to irregular wave spectra and evaluates the resulting power mismatch losses. We develop a multi-physics framework that allows for an in-depth exploration of how OFPV configuration—including floater count, material, design properties, and panel orientation—affects hydroelastic response and power mismatch. The framework employs a two-dimensional mechanical model incorporating the hydro-elastic fluid structure interaction for very large floating structure (VLFS). The mechanical problem is solved in the frequency domain using a finite element (FE) method. Once the motion of the structure is obtained, the time-resolved tilt for every module in the structure is calculated. With this inclination angle, the incident irradiance and temperature of every module can be estimated, which are used to calculate the power output and consequently the mismatch and movement losses.

Since our analysis is quite focused on the hydroelastic response, we simplify the problem with several assumptions. We limit external loads to wave forces, omitting current-induced loads. This is because currents primarily exert in-line friction and drag forces on thin elastic structures, thereby affecting station-keeping [7], rather than power mismatch losses, which are mainly influenced by transverse loads. Furthermore, while the mooring and anchoring systems are vital to station-keeping [11], and structural fatigue is essential for durability assessment [14], these aspects lie beyond this study's scope since our emphasis is on the fluid–structure interaction and associated power mismatch losses.

Additionally, the designs presented in this work are academic and are not affiliated with any commercial entities. Therefore, we do not investigate a specific OFPV platform design. Instead we formulate a systematic engineering analysis and then investigate the impact of the structural properties in isolation on the power-mismatch losses. For example, through our analysis, we will answer fundamental questions such what happens when you double or half the thickness of the floater. By narrowing the focus to power mismatch related performance measure, this study aims to bridge the gap in the literature on the fundamental correlation between the hydroelastic response of OFPV platform to irregular sea-states and their power mismatch losses.

This work is structured as follows. The following Section 2 presents the methodology employed to solve the problem at hand. Section 3 outlines the inputs to the model. The structural and optoelectrical results for a base case are presented in Section 4. The variations to this base case and their effect on the results are discussed in Section 5. Finally, Section 6 concludes this work.

2. Methodology

This section explains the problem at hand and the methodology developed to solve it. The flowchart presented in Fig. 2 presents the steps undertaken. The following sections will dive into its details.

The first step consists on defining and solving the structural problem in Section 2.1. The output of this step will be the elevation at every position of the floater. It will be used to compute the tilt in Section 2.2, which serves as a link between the structural and optoelectrical models. The methodology of the latter will be presented in Section 2.3.

2.1. Hydroelastic fluid–structure interaction model (FE-FSI model)

The structural analysis of the floating PV platform involves a complex hydroelastic problem characterized by a two-way interaction between the fluid and the elastic structure. We conduct this analysis using a monolithic finite-element model for fluid–structure interaction, referred to as the FE-FSI model throughout this manuscript.

The monolithic formulation and the FE model used in this work are based on the detailed methodology presented in [15]. In this manuscript, we focus on a frequency domain analysis, because we are primarily interested in the steady-state solution. This section briefly outlines the final frequency domain governing equations and the FE model. The convergence, conservation, and validation analysis for this FE model, when applied to a similar problem involving a floating beam with joints, was previously presented in [15].

2.1.1. Definition of the boundary value problem

Fig. 1a presents the schematic of the boundary value problem. Here, the fluid domain is denoted Ω. It is bounded by the bottom boundary Γ_{sb}, the fluid free-surface Γ_{fs}, inlet Γ_{in} and outlet Γ_{out}. The floating PV platform is represented by the boundary Γ_b. The end points of this platform are denoted by Λ_e. This platform may be composed of multiple floaters, connected by joints, denoted by Λ_j. This boundary value problem involves three unknowns, (1) velocity potential ϕ defined on Ω, (2) free-surface elevation κ defined over Γ_{fs} and (3) transverse beam deflection η defined over Γ_b.

In the frequency domain formulation, the unknown quantities ϕ, η, and κ are assumed to be harmonic. Here, a space and time-varying quantity, say the beam deflection $\eta(t, \mathbf{x})$, is defined in terms of the excitation frequency ω and a time-independent quantity $\bar{\eta}(\mathbf{x})$ as

$$\eta(t, \mathbf{x}) = \bar{\eta}(\mathbf{x}) \exp(-i\omega t). \tag{1}$$

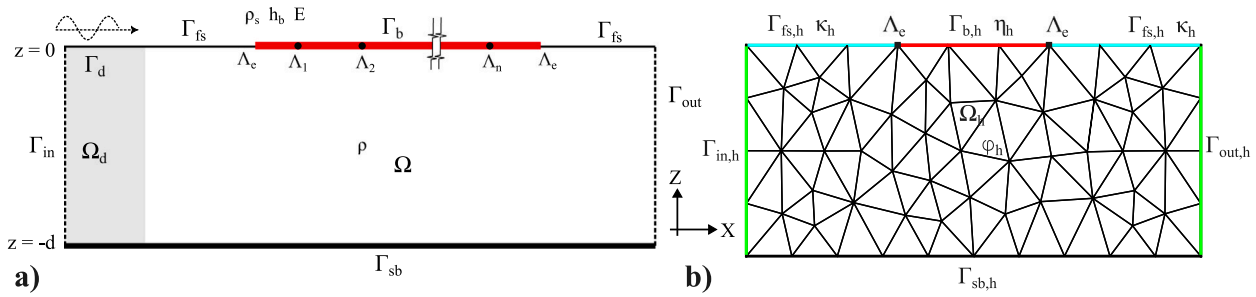

Fig. 1. (a) Schematic of the boundary value problem, consisting of the fluid domain Ω with constant water-depth d, bounded by the bottom Γ_{sb}, inlet Γ_{in}, outlet Γ_{out}, free-surface Γ_{fs} and the floating PV platform Γ_b. Here Λ_j represent the free-hinges in the floating PV platform.
(b) Sketch of the discretized geometric entities, with Ω_h representing the discretized fluid domain, and $\Gamma_{sb,h}$, $\Gamma_{in,h}$, $\Gamma_{out,h}$, $\Gamma_{fs,h}$ and $\Gamma_{b,h}$ representing the discretized boundaries. Consequently, ϕ_h, η_h and κ_h are the discrete solutions to the velocity potential, free-surface elevation and beam deflection, respectively.

Following this harmonic assumption, the governing equations for the time-dependent ϕ, η and κ get simplified to governing equations for time-independent $\bar{\phi}$, $\bar{\eta}$ and $\bar{\kappa}$. To simplify the notations in this section, we drop the over-bar hereafter, i.e., $\phi \overset{\text{def}}{=} \bar{\phi}$, $\eta \overset{\text{def}}{=} \bar{\eta}$ and $\kappa \overset{\text{def}}{=} \bar{\kappa}$.

We now present the coupled governing equations for the system in frequency domain formulation. Assuming inviscid, irrotational, and incompressible flow, the governing equation for the fluid flow within Ω is given by the potential flow theory Eq. (2).

$$\Delta\phi = 0 \qquad \text{in } \Omega. \tag{2}$$

The velocity potential ϕ is a scalar measure of the fluid velocity vector $\mathbf{u} = \nabla\phi$.

We formulate a boundary value problem by specifying conditions at the boundaries Γ of this fluid-flow domain Ω. We impose a no-flow boundary condition Eq. (3a) on the bottom boundary Γ_{sb}. The ocean wave input is given through the inlet boundary Γ_{in} using Eq. (3b), where $\mathbf{n}$ is the outward unit normal to the boundary and u_{in} is the inlet velocity prescribed using the Airy's wave theory [16, ch. 3]. At the outlet boundary Γ_{out}, we impose a radiation boundary condition Eq. (3c) for releasing the waves downstream of the floating PV platform.

$$\mathbf{n}\cdot\nabla\phi = 0 \qquad \text{on } \Gamma_{sb}, \tag{3a}$$

$$\mathbf{n}\cdot\nabla\phi = u_{in} \qquad \text{on } \Gamma_{in}, \tag{3b}$$

$$\mathbf{n}\cdot\nabla\phi = ik\phi \qquad \text{on } \Gamma_{out}. \tag{3c}$$

Here k is the angular wave-number for the ocean wave with frequency ω, obtained using the dispersion relationship Eq. (4), where d is the water depth at the inlet boundary.

$$\omega^2 = g\,k\,\tanh(kd). \tag{4}$$

The free-surface Γ_{fs} and beam Γ_b boundaries involve a kinematic and a dynamic boundary condition. The kinematic free-surface boundary condition Eq. (5a) on Γ_{fs} implies that the free-surface elevation moves at the vertical fluid velocity. The dynamic free-surface boundary condition Eq. (5b) on Γ_{fs} is used to impose atmospheric pressure $p_a = 0$ at the fluid free-surface.

$$\phi_z + i\omega\kappa = 0 \qquad \text{on } \Gamma_{fs}, \tag{5a}$$

$$i\omega\rho\phi - \rho g\kappa = 0 \qquad \text{on } \Gamma_{fs}. \tag{5b}$$

This is obtained using the linearized dynamic Bernoulli's equation, assuming a small free-surface elevation.

$$p = i\omega\rho\phi - \rho g\kappa. \tag{6}$$

Here g is the acceleration due to gravity and ρ is the density of the fluid. Therefore, the dynamic boundary condition Eq. (5b) is obtained by setting the pressure $p = p_a = 0$ along Γ_{fs}.

The kinematic boundary condition Eq. (7) on Γ_b is obtained assuming no gap between the deforming beam and the fluid-free surface underneath the beam.

$$\phi_z + i\omega\eta = 0 \qquad \text{on } \Gamma_b, \tag{7}$$

The dynamic boundary condition on Γ_b requires the introduction of the beam governing equations. The beam is modeled using the Euler–Bernoulli beam theory. Consider a beam with mass per unit area m_b and bending stiffness D_b. The transverse deflection η of this beam, under the action of transverse load p is given by Eq. (8).

$$-m_b\omega^2\eta + D_b\Delta^2\eta = p. \tag{8}$$

For a beam having a solid cross-section of thickness h_b, and made of material with density ρ_s and Young's modulus E, the mass per unit area is $m_b = \rho h_b$ and the bending stiffness is $D_b = EI_b$, where $I_b = \frac{1}{12}h_b^3$ is the second moment of area assuming a unit-width beam. For the floating beam, the transverse load is due to the pressure from the fluid underneath the beam. This is imposed by equating the transverse load in Euler–Bernoulli equation Eq. (8) with the pressure in the dynamic Bernoulli-equation Eq. (6), thus resulting in the dynamic boundary condition Eq. (9) on Γ_b.

$$-m_\rho\omega^2\eta + D_\rho\Delta^2\eta - i\omega\phi + g\eta = 0 \qquad \text{on } \Gamma_b. \tag{9}$$

Here $m_\rho = m_b/\rho$ is the normalized mass and $D_\rho = D_b/\rho$ is the normalized rigidity of the beam.

The beam governing equation requires the specification of its own boundary conditions on its endpoints Γ_e. In this manuscript, we restrict the analysis to free-edge boundary conditions. This is imposed by setting zero-moment and zero-shear conditions at these boundaries.

$$D_b\,\Delta\eta = 0 \qquad \text{on } \Lambda_e, \tag{10a}$$

$$\nabla(D_b\,\Delta\eta)\cdot\mathbf{n}_\Lambda = 0 \qquad \text{on } \Lambda_e. \tag{10b}$$

Here $\mathbf{n}_\Lambda$ is the outward unit normal for the beam edges Λ_e. In case the platform is composed of multiple floaters, we join the floaters using joints Λ_j. At these joints, we impose a free-joint condition by setting the bending moment at the joints to zero.

$$D_b\,\Delta\eta = 0 \qquad \text{on } \Lambda_j. \tag{11}$$

This completes the definition of the multi-physics boundary value problem. We additionally place a damping zone Ω_d adjacent to Γ_{in} for absorbing waves reflected by the floating PV platform. Refer to [15] for a detailed description of the wave generation and absorption.

2.1.2. Numerical formulation

The above-mentioned boundary value problem is numerically solved using a monolithic finite-element scheme, as defined in [15]. Here, the monolithic term implies that the coupled fluid–structure governing equations are formulated in a single coupled weak-form.

For the sake of completeness of the work, we describe the formulation of the FE problem. We refer to [15] for a more detailed description of the steps to reach this final form. Consider a functional space $\mathcal{V}$

defined in the domain Ω, with trace space $\mathcal{V}_{\Gamma_{\text{fs}}}$ on the free-surface Γ_{fs}, and trace space $\mathcal{V}_{\Gamma_{\text{b}}}$ on the beam boundary Γ_b. The weak form reads as follows: *Find* $[\phi, \eta, \kappa] \in \mathcal{V} \times \mathcal{V}_{\Gamma_b} \times \mathcal{V}_{\Gamma_{fs}}$ *such that*:

$$B_\omega([\phi,\eta,\kappa],[w,v,u]) = L_\omega([w,v,u]) \qquad \forall [w,v,u] \in \mathcal{V} \times \mathcal{V}_{\Gamma_{\text{b}}} \times \mathcal{V}_{\Gamma_{\text{fs}}}, \quad (12)$$

where, w, v, u are the test functions corresponding to ϕ, η, κ, respectively, and

$$\begin{aligned} B_\omega([\phi,\eta,\kappa],[w,v,u]) =& (\nabla\phi, \nabla w)_\Omega + (-i\omega\phi + g\kappa, \beta(u+\alpha w))_{\Gamma_{fs}} \\ & - (-i\omega\kappa, w)_{\Gamma_{fs}} + (m_\rho \eta_{tt} + \phi_t + g\eta, v)_{\Gamma_m} \\ & + (D_\rho \nabla^2 \eta, \nabla v)_{\Gamma_b}, \end{aligned} \quad (13)$$

$$L_\omega([w,v,u]) = (u_{in}, w)_{\Gamma_{in}} + (u_{out}, w)_{\Gamma_{out}}. \quad (14)$$

In Eqs. (13) and (14), we have used the notation $(a,b)_\Gamma$ to denote the integral operation, i.e., $(a,b)_\Gamma = \int_\Gamma a\, b\, d\Gamma$. The weak-form is solved in a discretized domain, as shown in Fig. 1b. We consider a triangulation Ω_h of the domain Ω, with conformal triangulation of the domain boundary, $\Gamma_{sb,h}$, $\Gamma_{in,h}$, $\Gamma_{out,h}$, $\Gamma_{fs,h}$ and $\Gamma_{b,h}$. We define the finite-dimensional finite element spaces for the velocity potential, free surface elevation, and beam deflection, $\mathcal{V}_h$, $\mathcal{V}_{\Gamma_{\text{fs}},h}$ and $\mathcal{V}_{\Gamma_{\text{b}},h}$, respectively, as follows:

$$\mathcal{V}_h = \left\{ w_h \in C^0(\Omega) : \ w_h|_K \in \mathbb{P}_r(K), \forall K \in \Omega_h \right\}, \quad (15)$$

$$\mathcal{V}_{\Gamma_{\text{fs}},h} = \left\{ w_h|_E : \ w_h \in \hat{\mathcal{V}}_h, \forall E \in \Gamma_{\text{fs},h} \right\}, \quad (16)$$

$$\mathcal{V}_{\Gamma_{\text{b}},h} = \left\{ w_h|_E : \ w_h \in \hat{\mathcal{V}}_h, \forall E \in \Gamma_{\text{b},h} \right\}, \quad (17)$$

In this manuscript, $\mathbb{P}_r(K)$ is the space of Lagrange polynomials of degree 4 in an element K in the 2-dimensional space of fluid domain Ω. On the other hand E are 1-dimensional facets, corresponding to boundaries Γ_b and Γ_{fs}. Using this notation, the final discrete form in the frequency domain reads: *Find* $[\phi_h, \eta_h, \kappa_h] \in \mathcal{V}_h \times \mathcal{V}_{\Gamma_{\text{b}},h} \times \mathcal{V}_{\Gamma_{\text{fs}},h}$ *such that*

$$\begin{aligned} & B_\omega([\phi_h,\eta_h,\kappa_h],[w_h,v_h,u_h]) = L_\omega([w_h,v_h,u_h]) \\ & \forall [w_h,v_h,u_h] \in \mathcal{V}_h \times \mathcal{V}_{\Gamma_{\text{b}},h} \times \mathcal{V}_{\Gamma_{\text{fs}},h}, \end{aligned} \quad (18)$$

with B_ω and L_ω as defined earlier.

The finite element formulation was numerically implemented in the *Julia* programming language [17], using the *Gridap* finite element library [18]. This library allows for a high-level implementation of the formulation, closely resembling the mathematical notations in weak form. The *Gridap* library efficiently assembles internal loops based on this notation-based expression, optimized for the high-performance *Julia* Just-In-Time (JIT) compiler. A comprehensive software implementation of *Gridap* can be found in [19]. These features facilitate rapid prototyping of the finite-element program and offer excellent computational performance. Notably, *Gridap* can assemble finite-element formulations over mixed dimensions and mixed orders. This capability is crucial because the monolithic floating beam problem requires a formulation over both a fluid domain and the attached beam surface. The program used to generate the results for this manuscript is similar to the registered *Julia* package [20].

The presented FE model has been thoroughly validated for problems involving floating beams with joints in our previous work [15]. This includes validation against a standard test case of a floating platform composed of beams with different properties, connected by either free or elastic joints [21]. The model was also validated against results for floating beams in irregular bathymetry [22] and against experiments involving a 2D rectangular plate floating in a 3D domain [23]. These validations demonstrate that the FE model is particularly suitable for studying the floating PV platforms considered in this manuscript.

2.2. Link between fluid–structure interaction and optoelectrical analysis

The FE-FSI model does a frequency domain analysis of the hydroelastic response of the floating solar platform to incoming ocean waves. This model yields complex-valued solutions for the unknowns, assuming unit amplitude waves, thereby encompassing information about both the amplitude and phase. However, to conduct the optoelectrical analysis, it is necessary to evaluate the time series of the tilt of each panel on the platform. This section describes the process of obtaining this time series of tilt for each photovoltaic (PV) panel. It is also summarized in Fig. 2.

The inputs required for the FE-FSI model include the platform properties and the description of the fluid domain. The model returns complex-valued solutions of the velocity potential ϕ throughout the fluid domain, free-surface elevation κ along the ocean free-surface, and transverse beam deflection η along the entire floating PV platform. The solution is obtained for the entire range of the ocean wave spectrum, assuming unit-wave amplitude. This solution is referred to as the complex-valued response-amplitude operator (RAO) $\text{RAO}(\mathbf{x}, \omega)$ for each point $\mathbf{x}$ and frequency ω. This RAO is computed for the given floating PV platform properties and sea-bed topography.

We next use these RAOs along with the environmental conditions to compute the time series of the tilt at each panel. We source the environmental conditions from KNMI, the Dutch Meteorological Institute [24]. The hourly mean wind speed is obtained from reanalysis dataset of meteorological measurements provided by the KNW KNMI North Sea Wind atlas [25]. This time resolution corresponds to the highest one we could find for the Dutch North Sea. Using the hourly mean wind speed, we calculate the hourly sea state. This is done by calculating the Philips constant, peak frequency and peakedness parameter of the JONSWAP spectra based on the wind speed, as described in [26].

We now have the structural response in frequency domain and the hourly sea-state as well. However, optoelectrical analysis requires a time-domain representation, as it depends on both irradiance and the local tilt of each panel at every time step. The irradiance information is obtained from measurements. For this study this information is given in Section 3. To compute the local tilt of each panel over time, the structural response must be transformed from the frequency domain to the time domain using the complex-valued RAOs and the hourly sea-state spectrum.

The hourly sea-state spectrum is first converted to a wave elevation time-series using an inverse Fourier transform procedure. This is done using 2401 frequencies in range $f \in [0, 2]$ Hz, with randomized phase for each frequency, as most of the wind-generate wave spectrum energy is contained in this interval. Since our cut-off frequency is 2 Hz, our sampling frequency is 4 Hz, as per the Nyquist sampling theorem. Therefore, the wave-elevation time-series is evaluated at $\Delta t = 0.25$ s. As the irradiance is not expected to vary significantly within this time-step, $\Delta t = 0.25$ s is adopted as the time resolution for the analysis. In order to obtain the local panel response, we utilize the complex-valued RAO to obtain the complex valued deflection $\eta(\mathbf{x}, t)$ at each panel. The corresponding the tilt is then calculated by taking its spatial derivative, i.e., $\theta(\mathbf{x}, t) = \frac{\partial}{\partial x}(\eta(\mathbf{x}, t))$. The deflection and tilt time-series can now be used for opto-electric and structural analyses. The above mentioned algorithm is summarized in Fig. 2 and in Algorithm 1. To capture annual variations in system response, the process is repeated hourly for the entire year.

2.3. Optoelectrical

Once the time series data for tilt measurements at each position along the beam is collected, the optoelectrical modeling phase begins. As varying tilts will affect the incident irradiance on the PV modules, the initial step consists of calculating this irradiance in Section 2.3.1. Section 2.3.2 will continue by implementing the most suitable module temperature model from the literature. Finally, the power output and system losses can be obtained using the approach in Section 2.3.3.

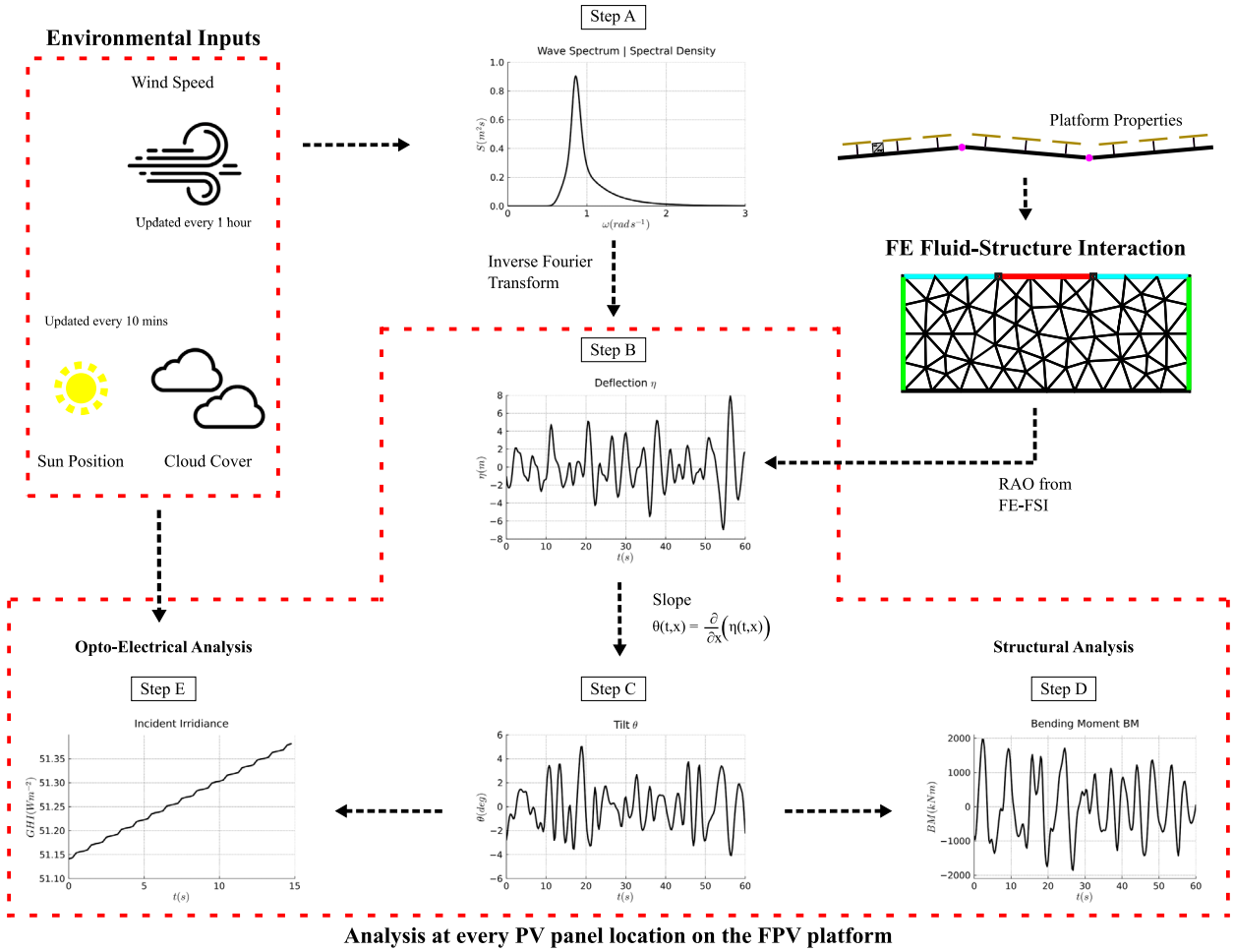

Fig. 2. Schematic of the solution procedure for the multi-physics problem.

2.3.1. Incident irradiance

The change in tilt affects the incident plane-of-array irradiance G_{POA} of a PV module [W m^{-2}], which was obtained with the isotropic Perez model [28] implementation of *pvlib* [29]. It consists of three components: the direct G_{dir}, diffuse G_{diff}, and ground-reflected G_{ref} irradiances. Their relation is expressed in Eq. (19).

$$G_{POA} = G_{dir} + G_{diff} + G_{ref} \tag{19}$$

These variables depend on the various components of solar irradiance: Global Horizontal Irradiance (GHI), Diffuse Horizontal Irradiance (DHI), and Direct Normal Irradiance (DNI). GHI represents the total irradiance received by a horizontal surface. This irradiance can be split into direct and scattered components. The direct component DNI is the irradiance that arrives straight from the sun to a surface normal to it. The sun altitude α_S tackles this difference in angle between the plane normal to the sun and the horizontal one. The diffuse component DHI represents the irradiance received by the horizontal surface scattered due to clouds and particles in the atmosphere. These three components are related as in Eq. (20).

$$\text{GHI} = \text{DHI} + \text{DNI} \cdot \sin \alpha_S \tag{20}$$

2.3.2. Module temperature

One key advantage of OFPV, leading to increased energy yield and system lifetime, is the lower module temperature caused by higher wind speeds and the heat sink behavior of the sea [30]. The operating efficiency of PV modules is higher when they function at a lower temperature.

The increase in yield depends on the local conditions and the system design [31]. This is reflected in the wide variety of results obtained by several researchers, in which the maximum difference in module temperature between FPV or land-based PV can range from 1.4 °C [32] to 12 °C [33]. Considering the impact of module temperature on PV power output and the varying results documented in the literature, special attention needs to be paid to modeling this quantity.

In literature, the most commonly used model to estimate the temperature of FPV systems is pvsyst's module temperature model [34] (see Eq. (21)). This model is derived from the heat balance proposed by Faiman [35] and its success lies in its simplicity.

$$T_C = T_{amb} + \frac{\alpha \cdot G_{POA} \cdot (1 - \eta_{mod})}{U_c + U_v \cdot ws} \tag{21}$$

Where T_C is the cell temperature [°Celsius], which will be used as module temperature T_M, T_{amb} is the ambient temperature [°Celsius], α is the absorption coefficient [-] (the default value of 0.9 will be used in this work), η_{mod} is the module power efficiency [-], U_c is the combined heat loss factor coefficient [W m^{-2} K^{-1}], U_v is the combined heat loss factor coefficient affected by wind [W s m^{-3} K^{-1}], and ws is the wind speed measured at a 10 meter height [m s^{-1}].

An overview of the U_c and U_v values of FPV systems in the literature has been provided in the review by Micheli [30, Table 1]. Considering the similarity in conditions and the OFPV system design, the study by Dörenkämper et al. [36] has been selected as a reference.

Dörenkämper et al. extracted the temperature coefficient of 5 FPV systems: 2 in the Netherlands and 3 in Singapore. Amongst these systems, the one denoted as NL2 is the most similar to this work. This system is closed (meaning that the back surface of the PV modules is

Data: Wind speed U_w updated every hour. Irradiance and temperature updated every 10 minutes.
Result: Structural analysis: Bending moment, shear force, and longitudinal stress within the platform. Optoelectrical analysis: time series of module temperature and power production.

Step A: Calculate the ocean-wave input for the hour
begin
- Calculate the values of significant wave height H_s and peak time-period T_p for fully developed sea-state from the hourly wind speed U_w, based on the approach described in [26].
- Calculate a JONSWAP spectrum [27] for these values of H_s and T_p to describe the wind-driven sea state. This spectrum is the power-spectral density function $S(\omega)\,[\mathrm{m^2\,s}]$, which measures the intensity of each wave frequency in the sea state.
- $U_w \rightarrow \left(H_s, T_p\right) \rightarrow S(\omega)$.

end

Step B: Compute the transverse deflection in the PV platform
begin
- Compute the transverse deflection time series from the input spectrum and RAO using inverse Fourier transform. Evaluate the time series for 1 h at the resolution of $\Delta t = 0.25$ s.
- $\eta(\mathbf{x}, t) = \sum_{j=1}^{j=n} \mathrm{RAO}(\mathbf{x}, \omega_j)\sqrt{2S(\omega_j)\Delta\omega}\exp\left(i(k_j\mathbf{x} - \omega_j t + \alpha_j)\right)$.
- Here, k_j is the wave-number for frequency ω_j, calculated using the dispersion relationship, while α_j is the uniformly randomized initial phase.

end

Step C: Get tilt time-series at each panel location
begin
- Compute slope time series at each location on the PV platform by taking the derivative of the deflection time series.
- $\theta(\mathbf{x}, t) = \frac{\partial}{\partial x}(\eta(\mathbf{x}, t))$.

end

Step D: Structural analysis
begin
- Use the tilt and deflection time series to compute the bending moment, shear force, and longitudinal stress within the platform.

end

Step E: Optoelectrical analysis
begin
- Use the tilt time series, along with the irradiance and ambient temperature (updated every 10 minutes), to calculate the module temperature and the power produced by the modules.

end

The wind speed information is updated every hour. Consequently, the algorithm is repeated every hour;

Algorithm 1: Algorithm for conducting the structural and optoelectric analysis of the floating PV system.

not directly exposed to the water surface), has a high footprint, can be categorized as a pontoon made of HDPE or similar material, and is located in the Netherlands. For this system, U_c is 25.2 $\mathrm{W\,m^{-2}\,K^{-1}}$ and U_v is 3.7$\mathrm{W\,s\,m^{-3}\,K^{-1}}$.

2.3.3. Power output

The power output of a PV module may deviate from the value indicated on the datasheet, which is specified under standard test conditions (STC). In operating conditions, the incident irradiance, temperature, and wind speed experienced by the PV module may vary. As a result, the power output will differ from the STC value. This environmental effect can be modeled by considering how the main electrical characteristics of a PV module are impacted. Therefore, Eqs. 20.4–20.5 and 20.21–20.22 from [37, ch. 20] have been implemented to model the effect of irradiance and temperature on the open circuit voltage V_{OC} [V], and short circuit current I_{SC} [A].

The power produced by each module is the maximum power point (MPP) of the current–voltage (IV) curve. This curve can be modeled using the ideal one-diode model expressed in Eq. (22) [37, ch. 20]. This equation ignores the effect of the series and shunt resistances.

$$I = I_L - I_0 \cdot (\exp \upsilon - 1) \tag{22a}$$

$$\upsilon = \frac{V}{V_{th} \cdot n \cdot N_S} \tag{22b}$$

where V_{th} is the thermal voltage equal to 25.85 mV and N_S is the number of cells in the module [-]. The unknowns of this equation, which are the light-generated current I_L [A], the dark saturation current I_0 [A], and the ideality factor n, can be found by evaluating the curve in the three points reported by the module manufacturer: the open circuit, the short circuit, and the MPP points.

$$I_{SC} = I_L \tag{23a}$$

$$0 = I_L - I_0 \cdot (\exp v_{OC} - 1) \tag{23b}$$

$$I_{MPP} = I_L - I_0 \cdot (\exp v_{MPP} - 1) \tag{23c}$$

By rearranging these equations, one can express the voltage as a function of the current relying only on the known parameters, obtaining Eq. (24a). The ideality factor n is found by iteratively solving Eq. (24b). This curve is computed for each series-connected module, and the voltages are added up to obtain the system's IV curve. By finding the MPP point of this curve, one can estimate the DC power output of the system P_{sys} [W].

$$V = \frac{n \cdot N_S \cdot k_B \cdot T_{STC}}{q} \cdot \ln\left(\left(1 - \frac{I}{I_{SC}}\right) \cdot (\exp v_{OC} - 1) + 1\right) \tag{24a}$$

$$I_{MPP} = I_{SC} \cdot \left(1 - \frac{\exp v_{MPP} - 1}{\exp v_{OC} - 1}\right) \tag{24b}$$

When each module operates at its MPP, like when connected to an optimizer with an MPP Tracker (MPPT), the system's DC power output is the sum of P_{MPP} of each module. Due to the high cost associated with this approach, it is common to connect the PV modules in series before pairing them with an inverter. Since the MPP conditions of each module will differ due to the varying incident irradiance, not all modules will operate at ideal conditions and the system DC power output will be lower than when using the MPPT strategy. The losses associated with this phenomenon are the power mismatch losses, which in the context of this research, are caused by the different tilts and orientations of the series-connected modules positioned along the structure.

By comparing the produced power output by the series-connected floating system $P_{floating}$ to the power produced by the system when each module is connected to an MPPT P_{MPPT}, the waves-induced mismatch power loss L_{mis} can be calculated using Eq. (25).

$$L_{mis} = (1 - \frac{P_{floating}}{P_{MPPT}}) \cdot 100\% \tag{25}$$

Similarly, one can quantify the power loss due to the movement of the waves as in [6], where the power produced by a system subjected to waves is compared to that produced by a horizontal one P_{hor}. P_{hor} is P_{MPPT} with all modules placed at a tilt of 0°. These three scenarios are graphically represented in Fig. 3. The expression of the movement power loss is that of Eq. (26).

$$L_{mov} = (1 - \frac{P_{MPPT}}{P_{hor}}) \cdot 100\% \tag{26}$$

The optoelectrical formulation was numerically implemented in *Python* programming language, with the help of the PV library *pvlib* [29]. The library has been extensively applied in several works and validated under different conditions [38–40], ensuring the accuracy of the optoelectrical methodology.

3. Case study description

This section presents a hypothetical design of the floating PV platform. The proposed platform has a length of $L_p = 100$ m. It is constructed using High-density polyethylene (HDPE). For our analysis, we consider that HDPE has density $\rho_{HDPE} = 952\,\mathrm{kg\,m^{-3}}$, Young's modulus $E_{HDPE} = 500$ MPa, and tensile yield strength of 27 MPa. The platform is divided into individual identical floaters, interconnected with free joints, as shown in Fig. 3. The weight of the auxiliary connectors is ignored in the present analysis.

Table 1
Table listing the properties for the base case PLA.

Property	Symbol	Value
Floater beam thickness	h_b	0.20 m
Cross-section Moment of Inertia per unit width	$I = \frac{1}{12} h_b^3$	6.667×10^{-4} m^3
Young's Modulus	$E = E_{HDPE}$	500 MPa
Mass per unit area (incl. PV modules)	m	192.956 kg m^{-2}
Characteristic hydro-elastic length Eq. (28)	λ_c	15.076 m
Floater orientation	A_z	180° (South)

GA-F200T c-Si PV modules [41] are selected due to their flexibility which facilitates their placement on a floating structure without impeding the structure's deformation or adding any resistance. The weight of the PV modules is negligible compared to that of the platform, even if they were not lightweight modules.

The PV modules are placed horizontally on top of the floating platform. This decision is made to ensure that the mechanical stability of the platform is not compromised by wind load, although optimal production would require the PV modules to be tilted. The modules are placed in a landscape orientation relative to the platform at a regular spacing of 2 m between the center of the panels. Therefore, a total of 50 modules are connected in series. Since the modeling is done in two dimensions, the sea waves income parallel to the string of modules to emphasize the mismatch losses experienced by the modules.

We examine several scenarios, varying the number of floaters, the thickness of the floaters, and the rigidity of the floaters. We first examine the case of floaters having a solid rectangular cross-section, assumed to be a beam thickness of $h_b = 0.20$ m, denoted as case PLA. The 100 m long platform is divided into a number of floaters, ranging from a single floater $NF = 1$ of length $L_f = 100$ m (PLA-NF01), to $NF = 50$ of length $L_f = 2$ m each (PLA-NF50). The platform characteristics for PLA are summarized in Table 1. The platform properties form the required input for the FE-FSI model.

The analysis is conducted for the PV platform floating in an offshore environment with a water depth $d = 30$ m. The temperature and wind data were obtained for a location in the North Sea near the coast, with coordinates 53° 24′42"N, and 6° 11′57"E for the year 2017. The data was taken from the KNW KNMI North Sea Wind atlas [25], which is a public reanalysis dataset of meteorological measurements. Specifically, we have taken the dataset named *KNW-CSV-TS-UPDATE* at the ID *064-116*. The GHI was not measured offshore thus it was taken from the nearest ground station, 160 km from the offshore location. The dataset was sourced from KNMI dataset of automatic weather stations in the Netherlands [42]. Specifically, we have taken the dataset named *Actuele10mindataKNMIstations* at station-ID *277*. Assuming that this irradiance data is valid for offshore conditions can lead to some discrepancies in the results. However, we expect this impact to be relatively small, especially in an annual analysis. Moreover, in a flat country like the Netherlands, irradiance generally has a low geographical daily variability.

The wind data is updated hourly and serves as the input for obtaining the hourly JONSWAP ocean-wave spectrum [27]. The wave-spectrum input along with the complex-valued hydro-elastic response from the FE-FSI model will then provide the tilt of each panel at a resolution of 0.25 s, as summarized in Section 2.2. The temperature and irradiance data are updated every 10 min. These are the inputs for the optoelectrical model. These environmental parameters are interpolated to match the 0.25 s resolution of the tilt using cubic spline interpolation. Applying the BRL model [43], the components of DNI and DHI are derived from the GHI. Despite the weather data not originating from an offshore location, it is presumed that the irradiance profiles observed along the coast are comparable to those encountered in offshore settings, providing a reasonable representation.

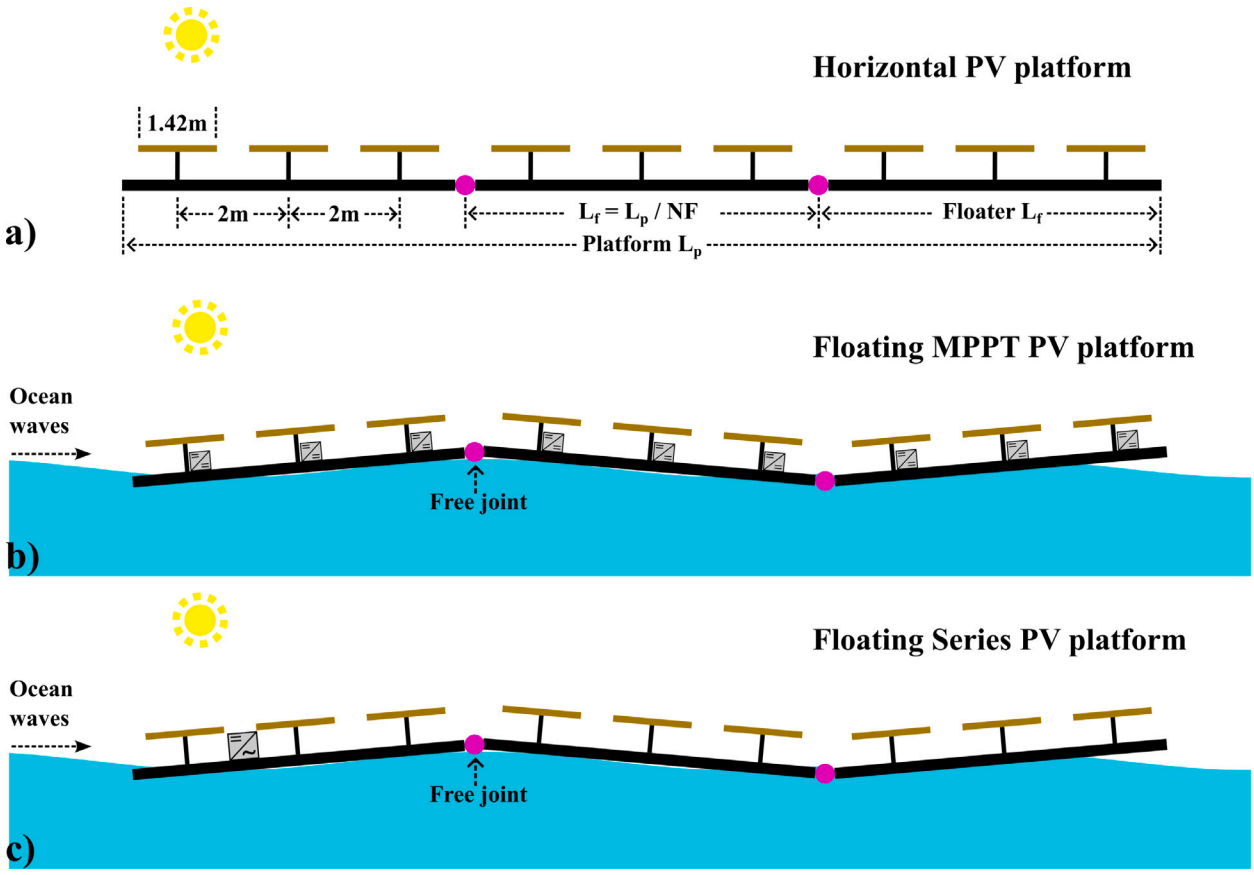

Fig. 3. Schematic of the floating PV platform. (a) Horizontal PV platform not subjected to the movement of waves. (b) Floating PV platform, with individual optimizers containing an MPP tracker and a DC–DC converter for each PV module. (c) Floating PV platform with all the modules connected in series and a single central inverter.

4. Numerical results: Base case

4.1. Setup of the numerical domain

The structural analysis of the floating PV platform is carried out using the monolithic FE-FSI model from Section 2.1. The presented FE model is capable of solving 2D and 3D problems, as demonstrated in [15]. However, in this manuscript, we restrict ourselves to a 2D analysis in the vertical plane. We consider a rectangular numerical domain, with a constant water depth of d and total length of $5.5L_p$, spanning between $x \in [-4L_p, 1.5L_p]$, where L_p is the length of the floating platform. The floating PV platform is placed in $x \in [0, L_p]$. The wave input is prescribed using the inlet boundary Γ_{in}. We additionally place a wide damping zone between $x \in [-4.0L_p, -0.5L_p)$ for absorbing any waves reflected by the floating PV platform.

This numerical domain is discretized using 4th order rectangular elements, with constant $\Delta x = 0.01L_p$, while the vertical mesh size varies exponentially from $0.48d$ near the bottom to $0.04d$ near the free-surface, to capture the high-gradients near the free-surface. The choice of 4th order polynomial basis functions enables us to use coarser mesh size and also allows us to compute the bending moments from the beam deflection. As per the convergence analysis from [15], the selected mesh size is notably smaller than necessary for capturing the beam deflection. However, our choice is dictated by the necessity to accommodate the highest wave frequency with non-zero amplitude in the chosen wave spectrum.

4.2. Platform response to monochromatic waves

The above-mentioned numerical setup is used to calculate the complex-valued response of the floating PV platform. We first investigate the case PLA-NF01 (see Section 3), which is made of a single floater of length $L_f = L_p = 100\,\text{m}$. We study the response of PLA-NF01 to wave-frequency $\omega = 1.5\,\text{rad}\,\text{s}^{-1}$ and wave-amplitude $\kappa_0 = 1\,\text{m}$. Fig. 4a-b present the solution obtained from the FE-FSI model for the beam deflection η, free-surface elevation κ and the velocity potential ϕ in the fluid domain. It should be noted that the FE model returns a complex-valued solution for all unknowns, thus containing information about both the amplitude of the response and the phase of the response.

For the purpose of the floating PV analysis, we are primarily interested in the deflection η of the beam. In Fig. 5, we present the magnitude of the complex-valued solutions for deflection, slope, bending moment, and shear force, along the length of the platform. The results are presented for two wave excitation frequencies $\omega = 1.5\,\text{rad}\,\text{s}^{-1}$ and $\omega = 2.0\,\text{rad}\,\text{s}^{-1}$. These frequencies were selected to demonstrate the significant impact that excitation frequency can have on the structural response. In each sub-figure of Fig. 5, we compare the results for cases PLA-NF01, PLA-NF05, and PLA-NF25 (see Section 3), thus showing the influence of changing the number of floaters in the platform.

Let us first analyze the response for the single floater case PLA-NF01. The solution in Fig. 5a-b highlights that the magnitude of deflection of the beam is maximum at the endpoints. Secondly, the magnitude of the motion is larger for the lower frequency $\omega = 1.5\,\text{rad}\,\text{s}^{-1}$ compared to $\omega = 2.0\,\text{rad}\,\text{s}^{-1}$. However, in both cases, the response in the leading and the trailing portion of the platform is quite similar.

Next, we study the response for the 5-floater case PLA-NF05. In this case, the free joints connecting the floaters are located at $x \in \{0.2L_p, 0.4L_p, 0.6L_p, 0.8L_p\}$. In Fig. 5a-b, we observe distinct cusps at these locations, along with local peaks in the magnitude of the deflection. This highlights that the heave motion of the platform is maximum at the endpoints and the free joints. Once again, the overall response of the platform PLA-NF05 is lower for the frequency $\omega = 2.0\,\text{rad}\,\text{s}^{-1}$ compared to $\omega = 1.5\,\text{rad}\,\text{s}^{-1}$. However, for $\omega = 2.0\,\text{rad}\,\text{s}^{-1}$, we can notably

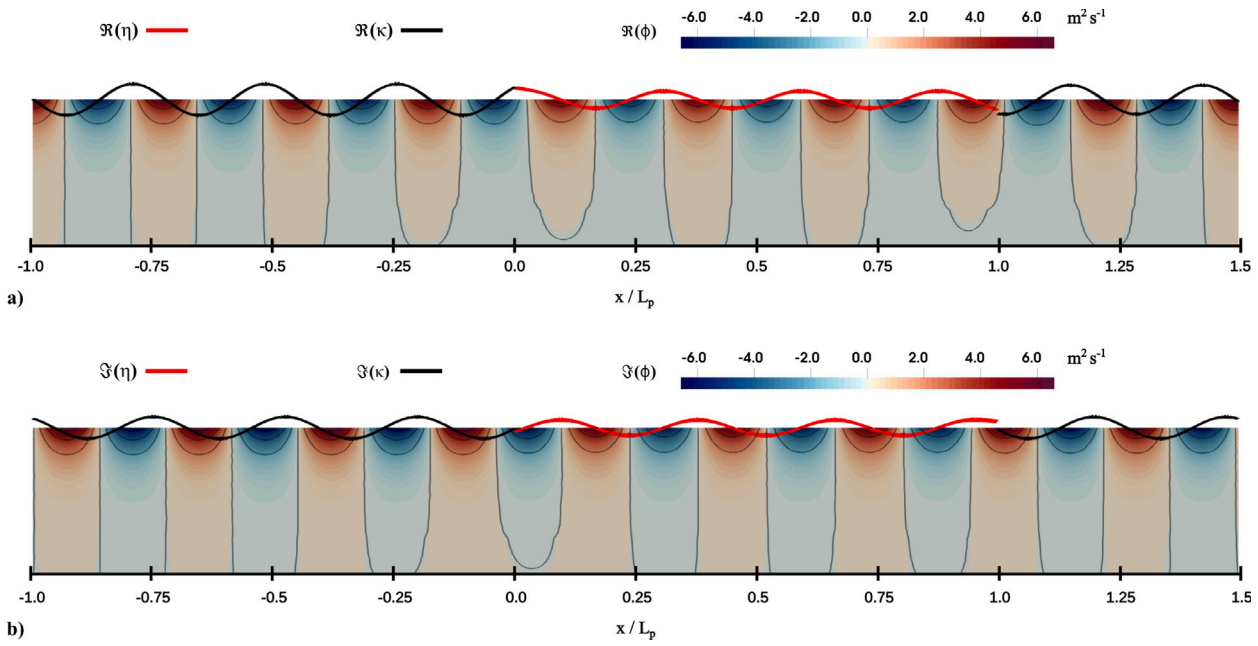

Fig. 4. Contour plot of ϕ and line plots of κ and η, obtained from the FE-FSI model, due to the interaction of PLA-NF01 platform with ocean wave of frequency $\omega = 1.5\,\mathrm{rad\,s^{-1}}$. (a) Real values of the solution. (b) Imaginary values of the solution.

observe that the magnitude of the response is larger in the upstream portion of the platform compared to the downstream portion. This is due to the partial reflection of the incoming waves by the platform, resulting in a gradual decrease in the wave energy propagating along the length of the platform.

Finally, we consider the case PLA-NF25 with 25 floaters. Fig. 5a-b once again highlights cusps and local peaks at the joints, consistent with the previous observation. However, here the response for $\omega = 2.0\,\mathrm{rad\,s^{-1}}$ is notably higher compared to $\omega = 1.5\,\mathrm{rad\,s^{-1}}$. Finally, there is no notable decay in the response in the downstream section of the platform, an indication of little reflection of the incoming wave energy for this frequency.

4.2.1. Tilt, bending moment, shear force and longitudinal stress

The complex-valued solution of deflection η can be used to calculate the tilt, bending moment, shear force, and longitudinal stress within the floater beams. The local tilt (θ) of the floater beam is given by Eq. (27a), the bending moment (BM) is given by Eq. (27b) and the corresponding shear force (V) in the cross-section is given by Eq. (27c). The longitudinal stress (σ) in the cross-section is calculated using Eq. (27d). Here y_c is the normal distance between the rotation axis for bending and the location on the cross-section.

$$\theta = \eta_x \tag{27a}$$

$$BM = EI\,\eta_{xx} \tag{27b}$$

$$V = EI\,\eta_{xxx} \tag{27c}$$

$$\sigma = BM\,\frac{y_c}{I} \tag{27d}$$

Fig. 5c-d present the magnitude of the complex-valued solution for slope (or tilt) along the length of the platform, for $\omega = 1.5\,\mathrm{rad\,s^{-1}}$ and $\omega = 2.0\,\mathrm{rad\,s^{-1}}$. Firstly, it is notable that for cases with joints, such as PLA-NF05 and PLA-NF25, a discontinuity in the slope is evident across the free joints. This behavior is expected, as the joints offer no bending resistance. Next, for PLA-NF01 and PLA-NF05, we note that the slope varies continuously within each floater, indicating the presence of an elastic response for the floater beam. In contrast, the plots for PLA-NF25 show a nearly constant slope within each platform. This indicates that the response of PLA-NF25 for both $\omega = 1.5\,\mathrm{rad\,s^{-1}}$ and $\omega = 2.0\,\mathrm{rad\,s^{-1}}$ is not elastic.

Table 2
Table listing the mean of the magnitude of the shear-load on the joints.

Case	$\omega = 1.5\,\mathrm{rad\,s^{-1}}$	$\omega = 2.0\,\mathrm{rad\,s^{-1}}$
PLA-NF05	13.45 kN	15.74 kN
PLA-NF25	0.83 kN	2.39 kN

In Fig. 5e–f we report the magnitude of the complex-valued solution for bending moment along the length of the platform, for $\omega = 1.5\,\mathrm{rad\,s^{-1}}$ and $\omega = 2.0\,\mathrm{rad\,s^{-1}}$. The bending moment is reported assuming unit width platform and unit-slope wave input $k\,\kappa_0 = 1$. Here k is the wave number for ocean-wave frequency ω, obtained from Eq. (4). For the corresponding cases, Fig. 5g-h report the magnitude of shear force $|V|$ and Fig. 6 reports the magnitude of longitudinal stress σ at $y_c = h_b/2$ in the cross-section of the floater beam. We obtain zero bending moment at the end points of the platform because of the application of free-edge boundary condition. Also, given our choice of free joints, we obtain zero bending moment at the joints for cases PLA-N05 and PLA-N25. The structural response for PLA-N01 and PLA-N05 exhibit significant bending moment, shear force, and longitudinal stresses, indicating strong elastic behavior. On the other hand, the 25-floater PLA-NF25 is observed to have a relatively small bending moment, indicating a largely rigid body response. Further, the bending moment and stresses for case PLA-NF05 once again highlight the gradual decay in the structural response along the length, owing to the partial reflection of the incoming waves by the platform.

The shear force plot in Fig. 5g-h also provides us with information about loads on the joints connecting the floaters in the platform. PLA-NF05 consists of 4 joints, at $x/L_p = \{0.2, 0.4, 0.6, 0.8\}$. The magnitude of shear load on these joints is given by the value of plot at these four locations. In Table 2, we report the mean of the load at these 4 joints. Similarly, we can obtain the magnitude of the loads at the 24 joints in PLA-NF25. The mean of these loads at the 24 joints of PLA-NF25 is also listed in Table 2 for the tested frequencies $\omega = 1.5\,\mathrm{rad\,s^{-1}}$ and $\omega = 2.0\,\mathrm{rad\,s^{-1}}$.

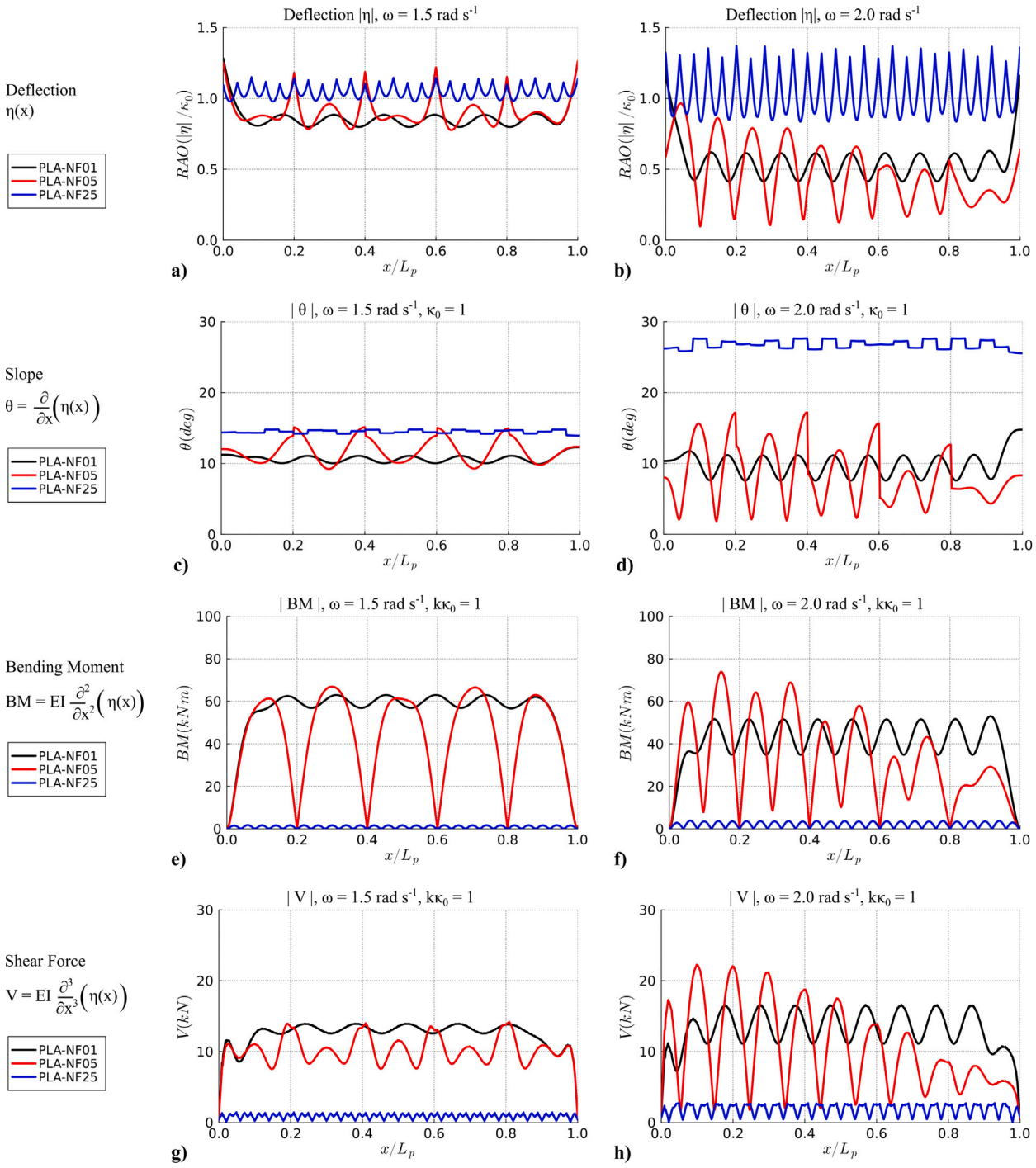

Fig. 5. Plots of the structural response of PLA-NF01, PLA-NF05 and PLA-NF25 floating platforms to monochromatic ocean-wave excitation of $\omega = 1.5\,\mathrm{rad\,s^{-1}}$ and $\omega = 2.0\,\mathrm{rad\,s^{-1}}$. (a–b) Magnitude of beam deflection and (c–d) magnitude of tilt, along the length of the platform. (e–f) Magnitude of bending moment (BM) and (g–h) magnitude of shear force in the cross-section, per unit beam-width for unit-slope wave excitation.

4.3. Response for a wide range of monochromatic waves

In the previous section, we restricted the analysis to just two excitation frequencies. In this section, we repeat the analysis for a wide range of excitation frequencies to better understand the differences in the total structural response for 1, 5, and 25 floater cases.

We repeat the analysis for $\omega \in [0.5, 5.0]$, which corresponds to ocean-wave length $\lambda \in [2.5, 190]\,\mathrm{m}$ for the assumed water-depth $d = 30\,\mathrm{m}$. This results in the contour plot Fig. 7a, c, e for PLA-NF01, PLA-NF05 and PLA-NF25, respectively, which are analogous to Fig. 5a. In these contour plots, the x-axis is the position along the platform, the y-axis is the excitation frequency and the contour levels are for the magnitude of the complex-valued solution of beam deflection η. The arrows in the plots highlight $\omega = 1.5\,\mathrm{rad\,s^{-1}}$ and $\omega = 2.0\,\mathrm{rad\,s^{-1}}$, which were studied in the previous section. Similar contour plots are prepared for the calculated slope response, bending moment, and shear force.

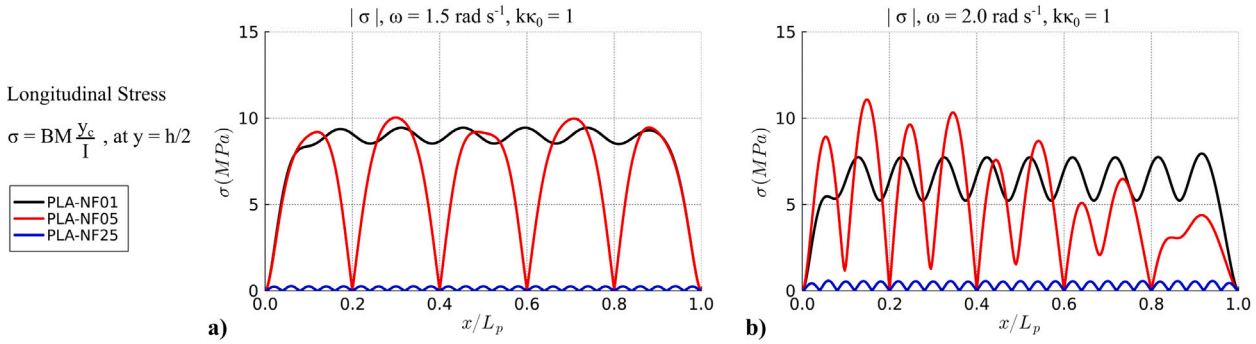

Fig. 6. Plots of the structural response of PLA-NF01, PLA-NF05 and PLA-NF25 floating platforms to monochromatic ocean-wave excitation of $\omega = 1.5\,\mathrm{rad\,s^{-1}}$ and $\omega = 2.0\,\mathrm{rad\,s^{-1}}$. (a-b) Magnitude of longitudinal stress in the cross-section, at $y_c = h_b/2$. Here y_c is the normal distance between the rotation axis for bending and the location on the cross-section.

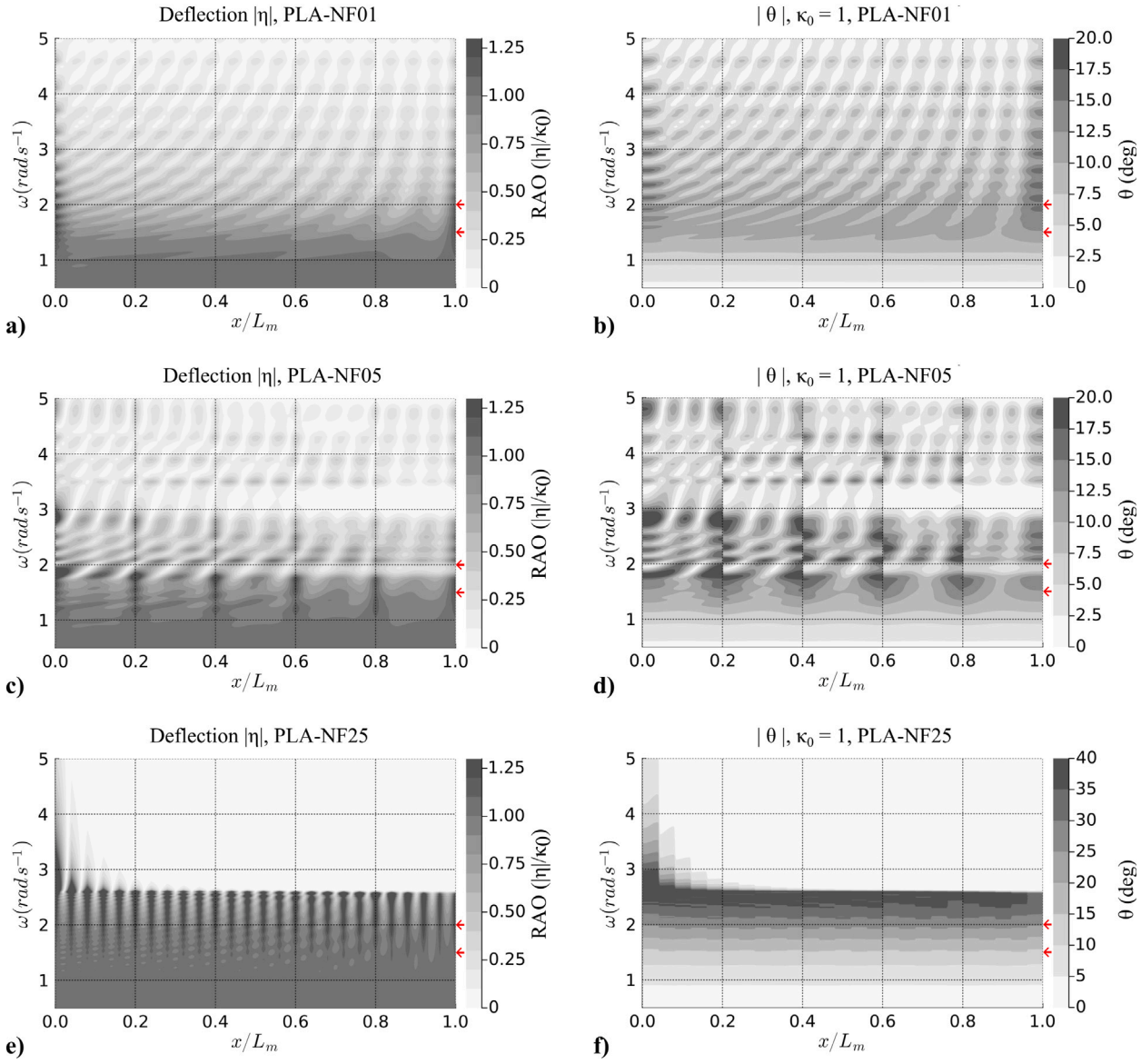

Fig. 7. Contour plots of the structural response along the length of the platform for ocean-wave frequency in range $\omega \in [0.7, 5.0]$. (a–b) Magnitude of deflection and slope for PLA-NF01. (c–d) Magnitude of deflection and slope for PLA-NF05. (e–f) Magnitude of deflection and slope for PLA-NF25. The arrows indicate the two frequencies that were plotted in Fig. 6.

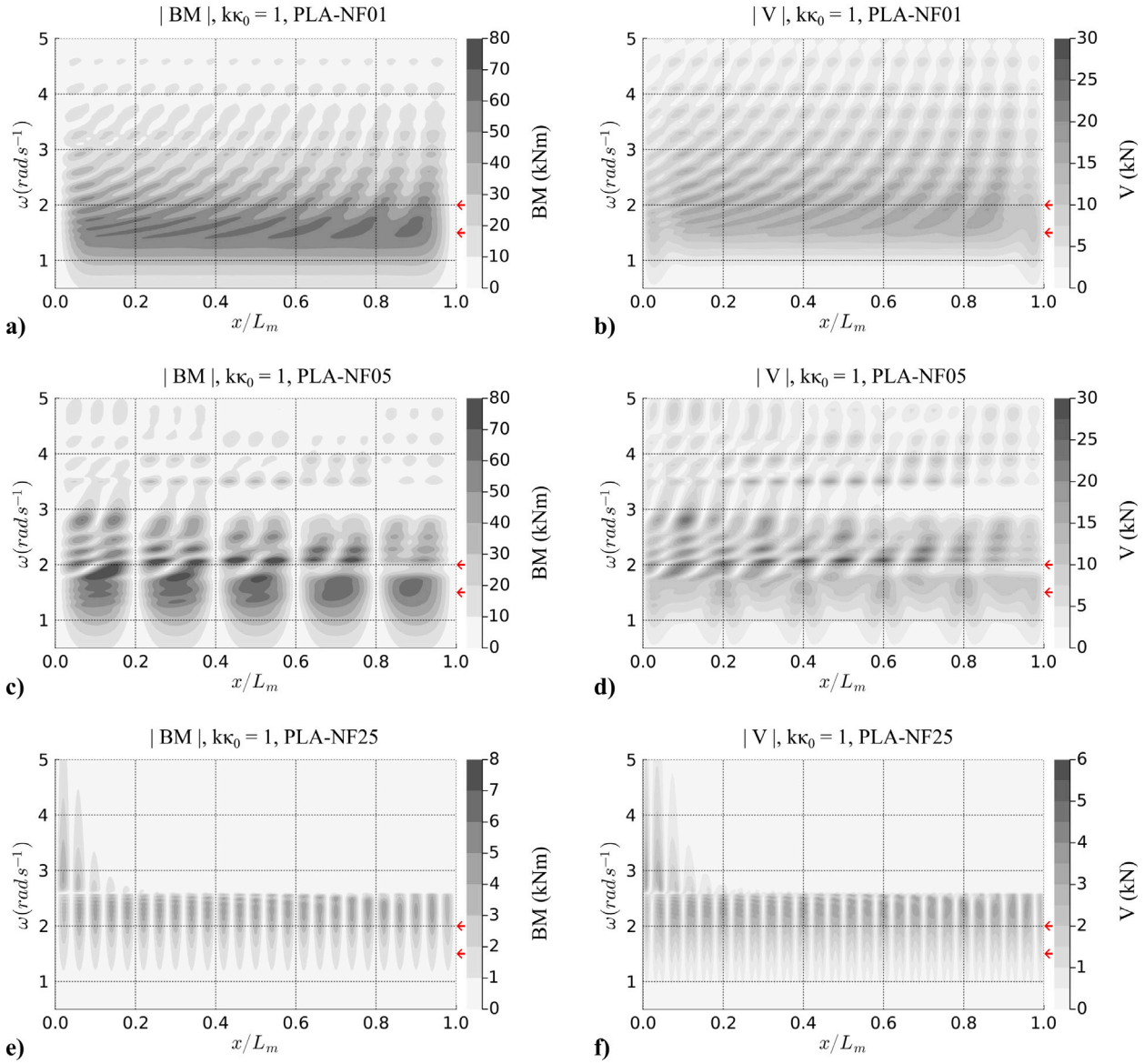

Fig. 8. Contour plots of the structural response along the length of the platform for ocean-wave frequency in range $\omega \in [0.7, 5.0]$. (a–b) Magnitude of bending moment and shear force for PLA-NF01. (c–d) Magnitude of bending moment and shear force slope for PLA-NF05. (e–f) Magnitude of bending moment and shear force for PLA-NF25. The arrows indicate the two frequencies that were plotted in Fig. 6.

The contour plots Fig. 7b, d, f present the magnitude of slope for unit-magnitude wave excitation. The contour plots Fig. 8a, c, e present the magnitude of bending moment for unit-slope wave excitation. Finally, the contour plots Fig. 8b, d, f present the magnitude of the shear force for unit-slope wave excitation. Note that the contour levels for PLA-NF25 are different compared to PLA-NF01 and PLA-NF05 across Fig. 7 and Fig. 8.

There are certain common observations across the plots, (1) the deflection magnitude is highest at the endpoints of the platform and at the free joints, (2) the slope is discontinuous at the free joints, (3) the bending moment and longitudinal stress are zero at the endpoints and the free joints.

In order to further explain the specific observations for each case, we recount the classification of the global response of floating structures in Fig. 9, based on the works of [44,45]. The response can be classified using two ratios, length of floater vs ocean-wave length L_f/λ, and length of floater vs characteristic hydro-elastic length L_f/λ_c. Here the characteristic hydro-elastic length λ_c is defined as Eq. (28) [44,45]. For the structural properties of PLA, given in Table 1, the characteristic hydro-elastic length $\lambda_c = 15.076\,\text{m}$.

$$\lambda_c = 2\pi \left(\frac{EI}{\rho g} \right)^{1/4} \tag{28}$$

In Fig. 9, we have indicated the response regime in which the 1, 5, and 25 floater cases are situated. For case PLA-NF01, the length of the floaters is the longest, i.e., both L_f/λ_c and L_f/λ are large. This indicates a very flexible floating structure response, which is evident in the results. Fig. 8a shows a significant bending moment across the length of the platform and for all frequencies, thus highlighting the presence of the elastic response. This elastic behavior however provides a stiffness against the wave excitation, thus resulting in smaller motions, as seen in lower deflection magnitudes in Fig. 7a. Therefore, PLA-N01 is observed to have lower motions, but higher structural loads.

On the other hand, PLA-N25 with 25 floaters has the smallest values of L_f/λ_c and L_f/λ, suggesting a rigid body response. The deflection contour in Fig. 7e highlights that the motion of PLA-N25 is larger compared to PLA-N01. This motion of PLA-N25 is particularly large within the critical wave frequency range of $[0.5, 3]\,\text{rad s}^{-1}$, which encompasses

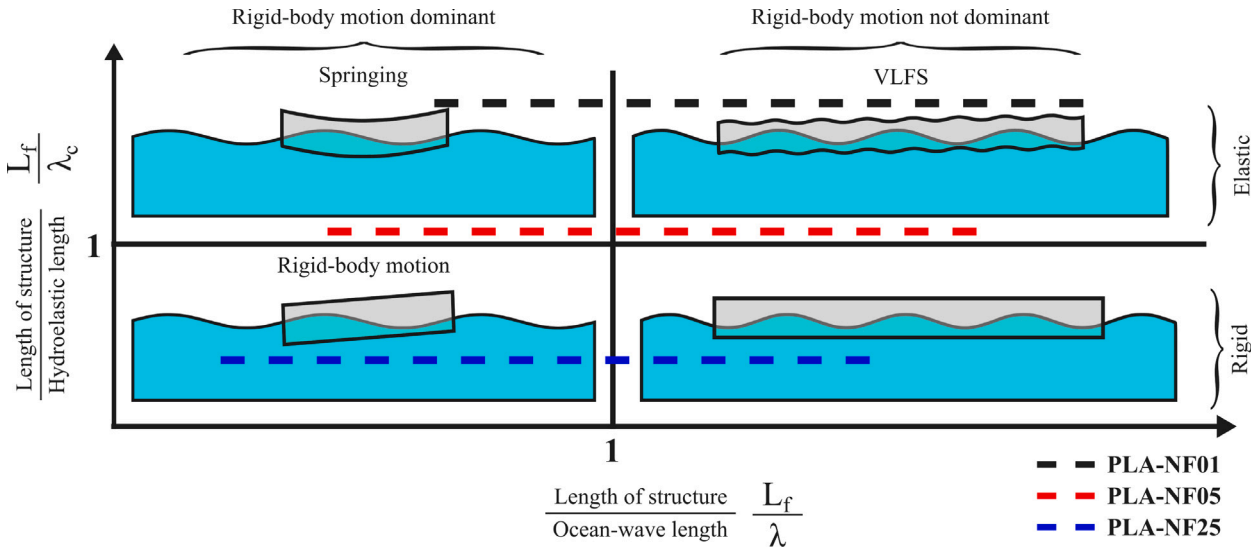

Fig. 9. Classification of the global response of floating structures [44]. The lines indicate the regime for PLA-NF01, PLA-NF05 and PLA-NF25.

the majority of fully developed wind-generated sea-states. The contour plot in Fig. 8e shows that the bending moment for PLA-N25 is at least one order of magnitude lower than PLA-N01 and PLA-N25. This indicates that a reduced elastic response leads to overall larger motions in the platform. Finally, we also observe that the leading floaters have higher magnitudes of motion, especially for high frequencies. This suggests that the leading floaters act as sacrificial barriers and reflect the incoming wave energy for the high frequencies. Overall, the PLA-N25 platform is expected to have large motion but smaller structural loads.

The case PLA-N05 has intermediate values of L_f/λ_c and L_f/λ. Fig. 7c and Fig. 8c show a larger magnitude of deflection and bending moment in PLA-NF05 compared to PLA-NF01. Hence this design choice would have worse motion and structural loads compared to PLA-NF01. Furthermore, the plots highlight a gradual decay of the response along the length of the platform due to successive partial reflection of the incoming wave energy.

Lastly, we examine the loads on the joints for cases PLA-NF05 and PLA-NF25. In Table 2, we provide the average magnitude of the loads across the joints, for two excitation frequencies. In Fig. 10, we present the average magnitude of loads for excitation frequency $\omega \in [0.5, 5.0]$. We also present the maximum magnitude of loads, among the joints. In general, we note that the PLA-NF25 has significantly lower loads on joints compared to PLA-NF05. Secondly, for low frequencies, the mean and maximum of the loads across joints is quite similar. However, for higher frequencies, notable differences emerge in the mean and maximum joint loads. This disparity arises due to the increasing reflection of higher frequencies along the length of the platform, resulting in higher loads in the upstream portion and lower loads in the downstream portion. This phenomenon is particularly pronounced in the case of PLA-NF25 for $\omega > 2.7\,\mathrm{rad\,s^{-1}}$, where the majority of the structural response is borne by the upstream floaters, leading to large loads on the upstream joints.

In summary, based on these observations, we can infer that increasing the number of floaters amplifies the platform motion. However, the structural loads exhibit a non-monotonic trend. This occurs because increasing the number of floaters results in a shorter length for each floater, causing the structural response to shift from elastic to rigid body behavior. Since structural loads depend on both the extent of the elastic response and platform motion, a non-monotonic trend emerges. Therefore, there is a trade-off in selecting the optimal number of floaters.

Finally, we would like to use these results to highlight the significance of the hydro-elastic natural frequency of the floating system. In Fig. 7, we can see that the response of PLA-NF25 peaks around $\omega = 2.8\,\mathrm{rad\,s^{-1}}$, response of PLA-NF05 peaks around $\omega = 1.95\,\mathrm{rad\,s^{-1}}$ and the response of PLA-NF01 peaks around $\omega = 1.5\,\mathrm{rad\,s^{-1}}$. These frequencies correspond to the natural hydro-elastic frequencies of the floaters, which are inversely proportional to the length of the floater. In the interest of brevity, we refrain from delving into the natural frequencies of the floating elastic system in this manuscript. However, the readers are directed to [46,47] for the discussions on the natural frequencies of such a floating elastic system.

4.4. Tilt distribution

As mentioned in Section 2.2, the tilt is the link between the structural and the optoelectrical models. Fig. 11(a) shows the standard deviation of the tilt along the platform for PLA with 1, 5, and 25 floaters. As expected from the previously presented results, the variation in tilt is larger for a higher number of floaters. In the case of 5 floaters, the highest deviation is experienced at the hinges of the platform and the lowest one at the center of the platform. In contrast, for the case of 25 floaters, the location of the hinges is not appreciated. The highest deviation is experienced at the beginning and the lowest one at the end of the platform. This is due to the already-mentioned effect of wave reflection. For the single floater case, the highest deviation is experienced at the extremes but it undergoes in general the lowest deviation in tilt. The modules at such unstable positions should be replaced by fake ones or glass to observe the same mechanical behavior without compromising the power output.

After having explored the variation of the tilt along the platform, Fig. 11(b) shows the distribution of tilt values over time at a specific position. One can observe again that the variation in tilt is larger for a higher number of floaters. In particular, while the tilt oscillates within a range of ± 10° for a single floater, it doubles to ± 20° when the platform is composed of 50 floaters. Along time, the tilt values oscillate around 0°; however, when fixing the time instant, the median values of the tilt along the platform may be positive or negative.

This greater variation in tilt for a higher number of floaters indicates that the power losses will also increase with the number of floaters. A wider variation in tilt translates into a greater range of irradiance values. This has a high influence on the power mismatch losses as the wider the range, the larger the losses.

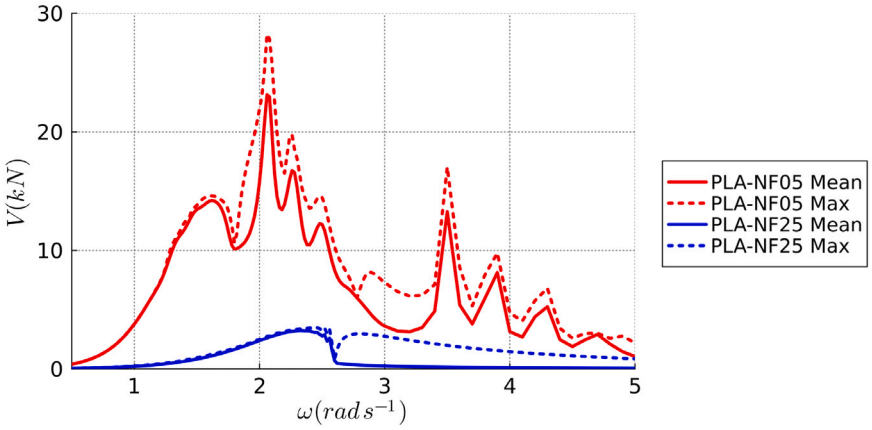

Fig. 10. Plot of the maximum and average values of the magnitude of shear force $|V|$ at the joints of cases PLA-NF05 and PLA-NF25, for unit beam-width and unit-slope wave excitation.

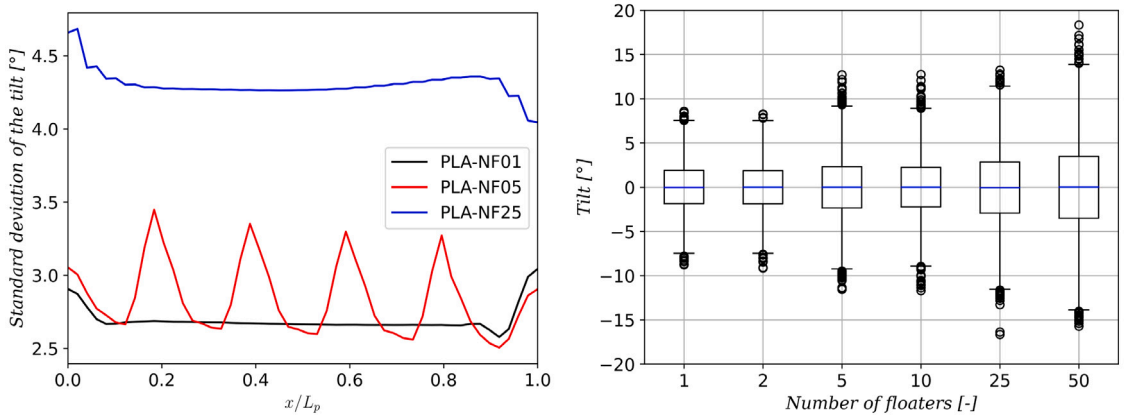

(a) (b)

Fig. 11. (a) Plot of the standard deviation of the tilt along the platform for PLA-NF01, PLA-NF05, and PLA-NF25. (b) Boxplot of the tilt values over time at $x = 0.19 \cdot L_p$ for an increasing number of floaters. Both figures considered the tilt from 9:00 to 10:00 on 1 January.

4.5. Power losses

The power output of the floating PV system is computed following the approach developed in Section 2.3. To obtain a time series of the tilt and azimuth, the negative tilts are transformed into positive ones after considering that the azimuth during those instants of time would be the opposite of that which the system faces.

Table 3 shows the annual energy yield for the OFPV system with a single inverter (referred to as *floating*), for the OFPV system with MPPT at the module level (*MPPT*), and for the one laying horizontally not subjected to the effect of waves (*horizontal*). These systems are facing South hence they are denoted as PLS. The values have been normalized to the nominal power of the system. As expected, the floating system produces the least of the three scenarios. In particular, the energy produced is 0.7% to 2.6% lower than when all modules are laying horizontally. The MPPT scenario generates slightly less energy than the horizontal scenario, with a difference ranging from 0.1% to 0.2%, depending on the number of floaters. Production decreases as the number of floaters increases, with the floating system being more impacted than the MPPT system. The horizontal scenario is not affected by the number of floaters.

The results from Table 3 can be better analyzed by computing the mismatch and movement losses. Fig. 12(a) shows how the mismatch losses experience an increase of 0.6% to 2.4% as the number of floaters increase, while the movement losses are almost negligible. The latter can be attributed to the fact that, on average, the oscillations are centered around 0°. Due to the wave effect, the modules will face the sun at one time instant, increasing productivity. However, at the next time instant, the modules will look away from the sun, decreasing the production. If each module produces at its MPP, any extra power generated at some time points is offset by lower power generation at others. Similar results were reported in [6].

Table 3
Annual energy yield for the floating, MPPT connected, and horizontal PV systems for different numbers of floaters.

Yield [kWh/W_p]	PLS-NF01	PLS-NF02	PLS-NF05	PLS-NF10	PLS-NF25	PLS-NF50
Floating	1.001	1.001	1.000	0.999	0.991	0.982
MPPT	1.007	1.007	1.007	1.007	1.007	1.006
Horizontal	1.008	1.008	1.008	1.008	1.008	1.008

This phenomenon can be seen in Fig. 12(b), which shows the power produced by the floating, MPPT, and horizontal systems on the day with the highest mismatch losses. The case of 25 floaters has been chosen as an example. The system with MPPT presents oscillations in power that are centered around the power produced by the horizontal system. With a higher magnitude of the oscillations and shifted down, one can encounter the power produced by the series-connected modules. In that same figure, the dip at around 11:30 shows the effect of a passing cloud on the power generation. The three systems produce a similar output during that cloudy instant since the mismatch losses occur mostly during sunny moments.

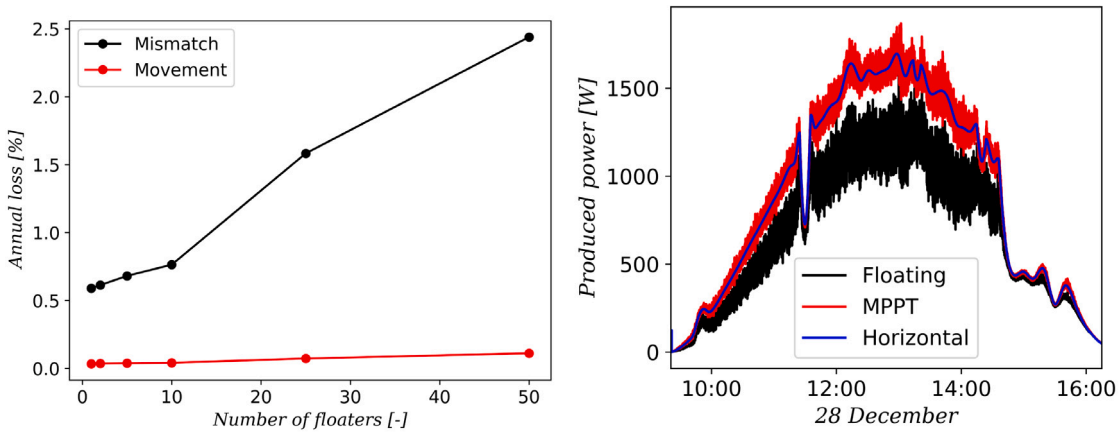

(a) (b)

Fig. 12. (a) Plot of the yearly mismatch and movement losses of PLS systems for an increasing number of floaters. (b) Plot of the power produced by the floating, MPPT, and horizontal PLS-NF25 systems on the day with the highest mismatch losses.

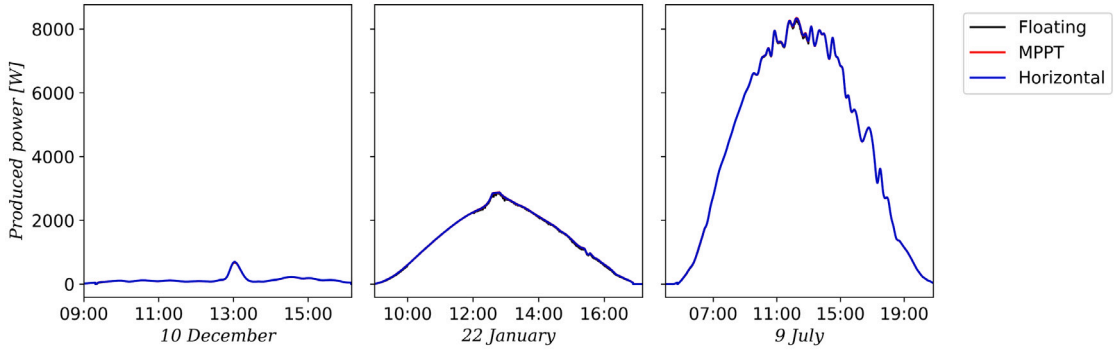

Fig. 13. Plot of the power produced by the floating, MPPT, and horizontal PLS-NF25 systems on selected days. December 10th is a cloudy windy winter day; January 22nd is a sunny not windy winter day; and July 9th is a sunny windy summer day.

Three phenomena explain why December 28th is the day with the highest mismatch losses. First, it is a sunny day. Mismatch losses are higher on sunny days when there is a high portion of DNI than on cloudy ones. Out of the three irradiance components explained in Section 2.3.1, the direct one G_{dir}, which is directly proportional to the DNI, is most affected by whether the module is facing the sun or not. Second, it is a windy day. The waves considered in this work are generated by wind. A stronger wind generates a higher tilt variation [6]. Third, it is a winter day. The mismatch is a relative value that depends on the power production. Since the production is higher in summer than in winter, the same losses will be relatively larger in winter than in summer.

For considerable oscillations to occur, all three phenomena must coincide simultaneously. It should be a sunny windy winter day. To showcase this, the power produced during three more days is plotted in Fig. 13. December 10th is a windy winter day but with a low DNI component. January 22nd is a sunny winter day but with a low wind. July 9th is a sunny windy day but during the summer. For the three days, the generation by the three cases under study is equivalent.

In terms of production, these findings are favorable as most of the losses will be reported during periods of low generation. These findings also add a benefit to the symbiosis between offshore photovoltaic and wind electricity, as the mismatch losses caused by a greater wind can be compensated by a higher production of wind power.

Before ending this section, we would like to comment on the tilt of the PV modules. To enhance the mechanical stability of the system, the modules have been placed horizontally on top of the platform. However, the optimal tilt for the North Sea is around 34° [48]. If the system under study were installed at this inclination, the mismatch losses would be relatively lower. The magnitude of the oscillations would remain similar, resulting in equivalent power loss. However, since the overall power production would be higher, the relative power loss would be smaller.

5. Variations to the base case

In this section, we systematically alter the characteristics of the base case PLA to analyze the impact of changing structural properties, such as Young's modulus, thickness and cross-section, and panel orientation on power mismatch losses.

5.1. Orientation

This subsection explores how the power losses are affected when the PV system faces East instead of South. Therefore, the system is denoted as PLE.

The movement and power mismatch annual losses for the two orientations are shown in Fig. 14(a). The movement losses experience the same increase from 0.1% to 0.2% for the two orientations. This indicates that orientation appears to have no appreciable impact on the annual yield in the case of the MPPT connection. The power mismatch losses stay in the range 0.6% to 2.6% for the two orientations. The losses are slightly lower for the East-facing system for platforms with 10 floaters or less, but higher for 25 floaters or more.

The distribution of mismatch loss for the two orientations, shown in the boxplots in Fig. 14(b) for an increasing number of floaters,

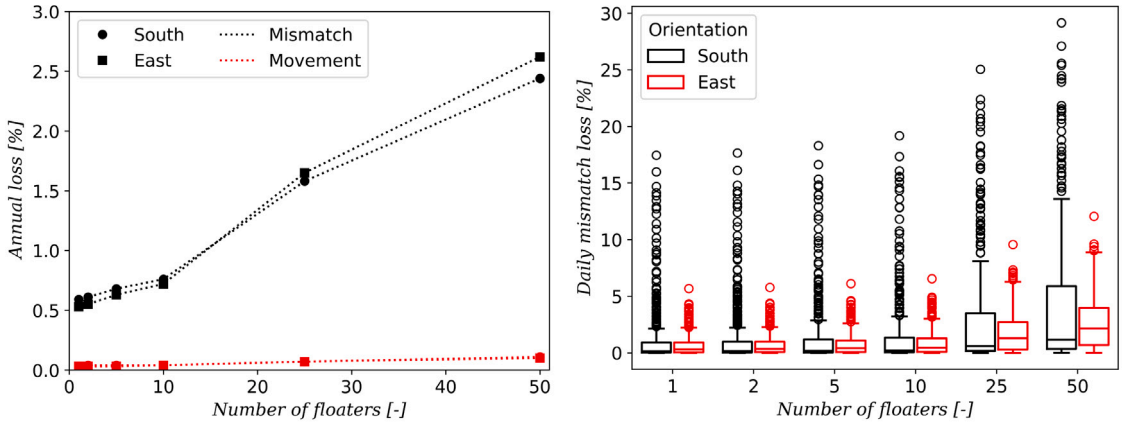

(a) (b)

Fig. 14. (a) Plot of annual power losses and (b) boxplots of the daily mismatch for the systems facing South (PLS) and East (PLE) for an increasing number of floaters.

shines a light on this behavior. The South-oriented system experiences a wider range of daily mismatch values, reaching on some days higher losses than the East-oriented system. For instance, the maximum daily mismatch loss of 1 floater is close to 18% for the South-oriented system but lower than 6% for the East-oriented system. This behavior occurs independently of the number of floaters. However, in terms of the median, the losses of the system facing East are higher. These systems experience the highest losses when they face the sun (in other words, when the sun's azimuth equals the system's orientation). Therefore, the South facing system will experience higher losses at noon while the East facing one will experience them in the morning and afternoon. Since the irradiance is higher during noon, the relative losses are more evenly distributed throughout the day for the East-facing system. This is because the mismatch losses are low when the irradiance is high and high when the irradiance is low. However, the difference in median values between the two systems depends on the number of floaters. For a low number of floaters, when the oscillations are small, the median loss for the two orientations is similar. The outlying values of the South-oriented system make that, throughout the year, the system experiences slightly higher losses. On the other hand, when the number of floaters is 25 or 50 and the oscillations are higher, the considerable difference in median loss between the two orientations compensates for the outlying daily losses of the South-oriented system. This makes that the East-oriented system experiences a higher annual mismatch loss.

The plots in Fig. 15 help understand this difference in the distribution of mismatch losses for the two orientations. Fig. 15(a) shows the power production on the day with the highest mismatch for the East-oriented case, January 14th. The power losses for this East-facing PV system occur mostly in the morning and afternoon instead of during noon as for the South-facing system. One can also note that this is again a sunny winter day. However, as opposed to December 28th, there is a drop in production near noon due to clouds passing.

The difference in orientation also affects the daily loss throughout the year, as shown in Fig. 15(b). A South-facing floater, which loses most of the power at noon, faces relatively high losses in the cold months when the days are short and most of the irradiance is centered around noon. An East-facing floater during those months is beneficial as most mismatch losses will occur when the irradiance is not so high. During the long summer days, the losses occurring at noon by the South-facing floater are not so detrimental because the irradiance is also high at noon. However, for the East-facing floater, the losses are relatively larger as the irradiance is still high in the hours around noon. However, the highest daily mismatch losses still occur in winter due to the higher wind speeds and lower produced power.

5.2. Young's modulus

We start with the base case PLA, as defined in Table 1, and vary only the Young's modulus of the material. We explore three scenarios: $E = 0.5\,E_{HDPE}$, $E = 1.0\,E_{HDPE}$, and $E = 2.0\,E_{HDPE}$. Fig. 16(a) illustrates the annual mismatch and movement losses, for platforms with various number of floaters, for these three values of Young's modulus. Fig. 16(b) presents the distribution of the daily mismatch losses.

From the plots, an interesting trend emerges, which can be explained, based on our analysis in Section 4. For 25 and 50 floaters, there is no discernible difference in the mismatch losses across the three Young's modulus values. In scenarios with a high number of floaters, the length of each floater L_f is small, resulting in small ratios L_f/λ and L_f/λ_c, indicative of a rigid body response. As observed earlier in Fig. 8e-f, under the rigid body response regime, the bending moment within the structure is minimal. This emphasizes that the bending stiffness of the beam has little influence on the structure's response, hence altering the Young's modulus of the material yields little difference in the mismatch losses.

Conversely, scenarios with a low number of floaters will have higher values of L_f/λ and L_f/λ_c, implying an elastic response. As per our observation in Fig. 8a-b, in these instances, the elastic response of the floater dominates. As a result, we observe distinct differences in the mismatch losses when the Young's modulus is altered for scenarios with a low number of floaters. Moreover, increasing the Young's modulus enhances the bending stiffness of the structure, thereby reducing the platform's motion and consequently diminishing the overall mismatch losses. This explains the observed reduction in losses with increasing Young's modulus, for cases with fewer number of floaters.

5.3. Thickness

In this section, we revisit the base case PLA, varying only the thickness of the beam. Case PLA has a thickness of $h_b = 0.2\,\text{m}$. We additionally test scenarios with thicknesses $h_b = 0.1\,\text{m}$ and $h_b = 0.4\,\text{m}$. Fig. 17(a) presents the annual mismatch and movement losses for platforms with 1–50 floaters, for these three floater thickness values. Fig. 17(b) presents the distribution of daily mismatch losses for the same thickness values. These plots reveal a curious trend. For scenarios with 1, 2, 5, and 10 floaters, an increase in platform thickness leads to a reduction in mismatch losses. However, for 25 and 50 floaters, an increase in thickness conversely results in increased mismatch losses.

The observation for fewer floaters is easily explained. In cases with fewer floaters, the structure operates in the elastic regime due to high values of L_f/λ_c and L_f/λ. Therefore, the elastic response dominates. Since the bending stiffness $EI \propto h_b^3$, an increase in thickness

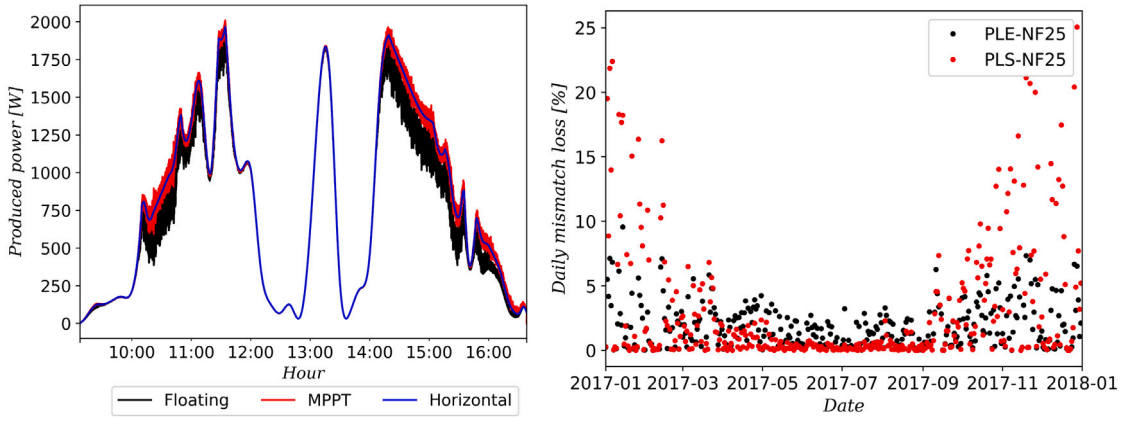

(a) (b)

Fig. 15. (a) Plot of the power produced by the floating, MPPT, and horizontal PLE-NF25 systems on January 14th, the day with the highest daily mismatch losses. (b) Daily mismatch throughout the year for PLE-NF25 and PLS-NF25.

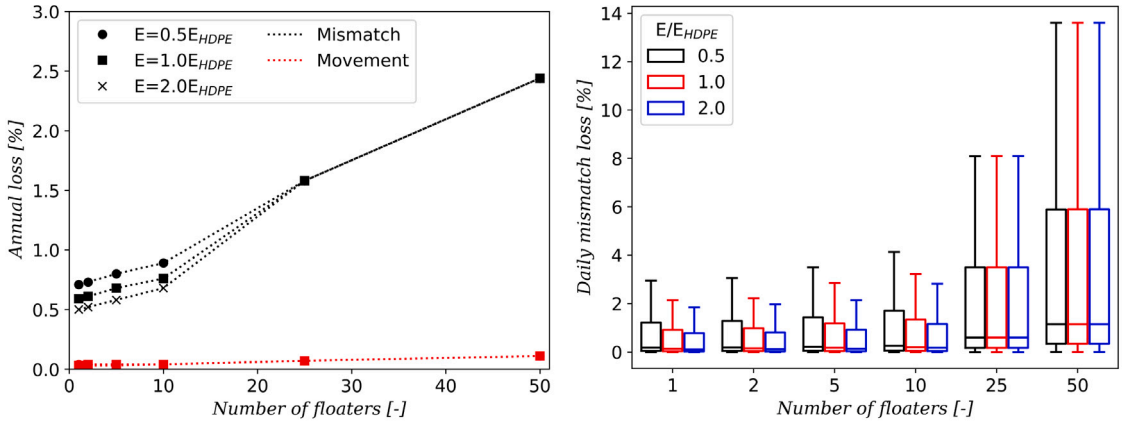

(a) (b)

Fig. 16. (a) Plot of annual power losses and (b) boxplots of the daily mismatch for systems with varying Young's modulus for an increasing number of floaters.

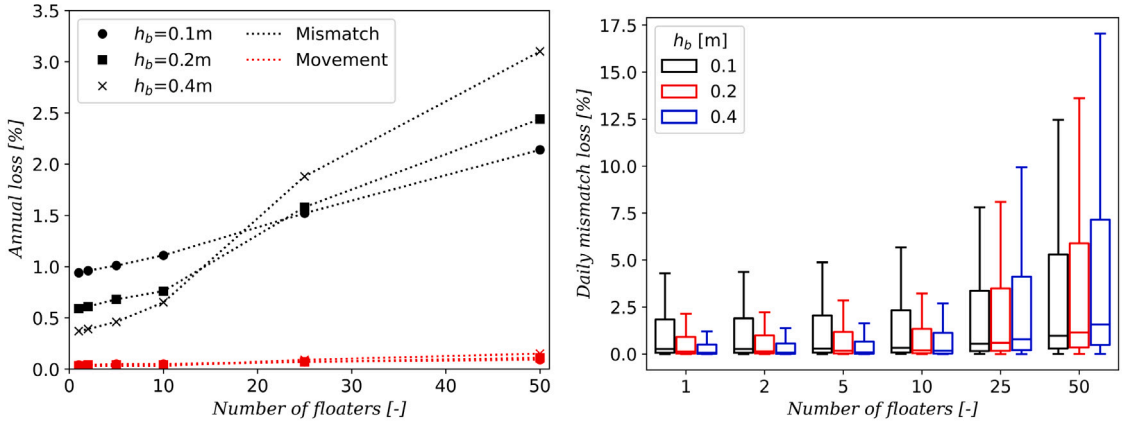

(a) (b)

Fig. 17. (a) Plot of annual power losses and (b) boxplots of the daily mismatch for systems with varying thicknesses for an increasing number of floaters.

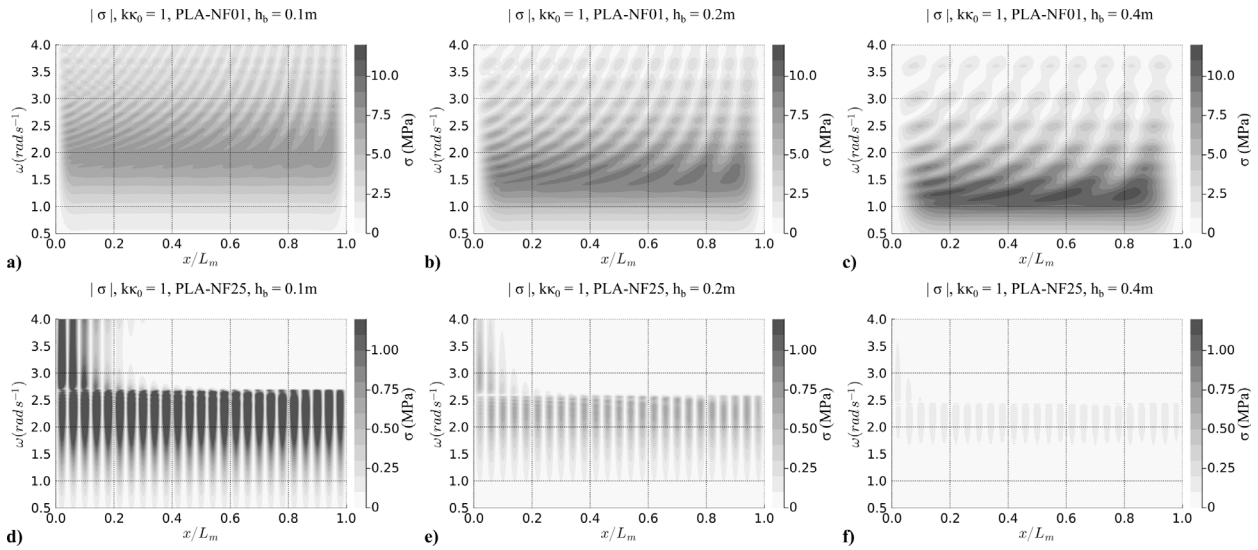

Fig. 18. Contour plots of the longitudinal stress in the floater beam cross-section. (a-c) PLA-NF01 with $h_b = 0.1\,\text{m}$, $0.2\,\text{m}$, $0.4\,\text{m}$. (d-f) PLA-NF25 with $h_b = 0.1\,\text{m}$, $0.2\,\text{m}$, $0.4\,\text{m}$.

significantly enhances the bending stiffness, resulting in substantially smaller motions for $h_b = 0.4\,\text{m}$ compared to $h_b = 0.1\,\text{m}$, thereby leading to lower mismatch losses.

The reversal of this trend for 25 and 50 floater scenarios can be explained by examining the influence of h_b on the characteristic hydro-elastic length of the structure, i.e., $\lambda_c \propto (h_b)^{3/4}$. For a given floater length L_f, changing the floater thickness alters the ratio $L_f/\lambda_c \propto (h_b)^{-3/4}$. Consequently, a thinner beam exhibits a higher L_f/λ_c, indicating an elastic-dominant response, while a thicker beam results in a lower L_f/λ_c, leading to a rigid body response.

This distinction is further supported by the contour plots of longitudinal stress in the floater cross-section, as presented in Fig. 18. In Fig. 18a-c, we present the contour plots of the magnitude of stress for a platform composed of a single floater of $L_f = 100\,\text{m}$ (PLA-NF01) with floater thicknesses h_b of $0.1\,\text{m}$, $0.2\,\text{m}$, and $0.4\,\text{m}$, respectively. In Fig. 18d-f, we present the contour plots of the magnitude of stress for a platform composed of 25 floaters of $L_f = 4\,\text{m}$ (PLA-NF25), with floater thicknesses h_b of $0.1\,\text{m}$, $0.2\,\text{m}$, and $0.4\,\text{m}$, respectively. In the PLA-NF01 scenario, there is significant stress across a wide range of excitation frequencies for all thicknesses, indicating elastic response. In the PLA-NF25 scenario, we observe nearly zero stress for the $0.4\,\text{m}$ floater, indicating a rigid body response; while strong stresses are observed for the $0.1\,\text{m}$ floater, indicating an elastic response.

As $h_b = 0.4\,\text{m}$ for PLA-NF25 has very little elastic response, there is no additional stiffness against wave excitation, resulting in large motions and mismatch losses for 25 and 50 floater cases. Conversely, $h_b = 0.1\,\text{m}$ exhibits significant elastic response even for 25 and 50 floater scenarios, providing additional stiffness against wave excitation and resulting in smaller motions and mismatch losses.

5.4. Fill ratio

In this test, we modify the cross-section of the floater. The base case PLA has a solid cross-section. We test scenarios, where the middle portion of the cross–section is hollowed out, to minimize weight with limited influence on the bending stiffness. We quantify this using a "fill ratio" γ. In addition to solid cross-section having $\gamma = 1$, we test cases with $\gamma = 0.5$ and the lightest $\gamma = 0.25$.

Fig. 19(a) presents the annual mismatch and movement losses for platforms with 1–50 floaters, for these three fill-ratio values. Fig. 19(b) presents the distribution of daily mismatch losses for the same. Similar to Section 5.3, the obtained trend is dependent on a interplay between rigid-body and elastic response, driven by the change in bending stiffness, mass and characteristic hydro-elastic length.

6. Conclusion

In this work, we have analyzed the interaction of an OFPV system with surface waves focusing on the structural loads of the platform and the mismatch losses experienced by the system. Using a combined framework to study this multi-physics problem, we have examined how the number of floaters, orientation, platform's Young modulus, thickness, and fill ratio affect the structural and optoelectrical response of the OFPV system. The main key findings are:

- A trade-off exists in selecting the number of floaters for an offshore floating PV system. From an optoelectrical perspective, minimizing motion is desirable to reduce the tilting of PV panels. This favors designs with a single or a few large floaters, such as PLA-NF05, which tend to exhibit smaller overall motions. However, such configurations typically operate within the elastic response regime, leading to higher structural stresses and potential fatigue-related issues. In contrast, using a larger number of smaller floaters, such as PLA-NF25, tends to shift the system response toward rigid-body behavior. This transition reduces elastic stresses in the floaters, mitigating structural concerns. However, these configurations experience greater tilting motion, which increases optoelectrical losses.
- The system orientation shows a limited effect on the mismatch losses. This was expected considering the original horizontal position of the PV modules. However, North–South oscillations are preferred over East–West oscillations as the losses in the latter case are relatively higher for most of the year except for winter.
- The structural properties of the platform can have a significant influence on the overall power mismatch losses. A change in Young's modulus, thickness, or cross-section of the floater beam can alter the hydro-elastic response from a rigid body response to an elastic dominant response. This influence depends on the number of floaters of the platform.
- The scenarios with up to 10 floaters were observed to have an elastic dominant response. As a consequence of this, the power mismatch loss is observed to reduce with an increase in Young's modulus of the material, with an increase in the thickness of the floater beam, or with an increase in the fill ratio for the cross-section.
- For the 25 and 50 floaters scenarios, we observed a rigid body response for all tested values of Young's modulus. Therefore, Young's modulus did not have a significant impact on the power mismatch losses. On the other hand, the 25 and 50 floaters

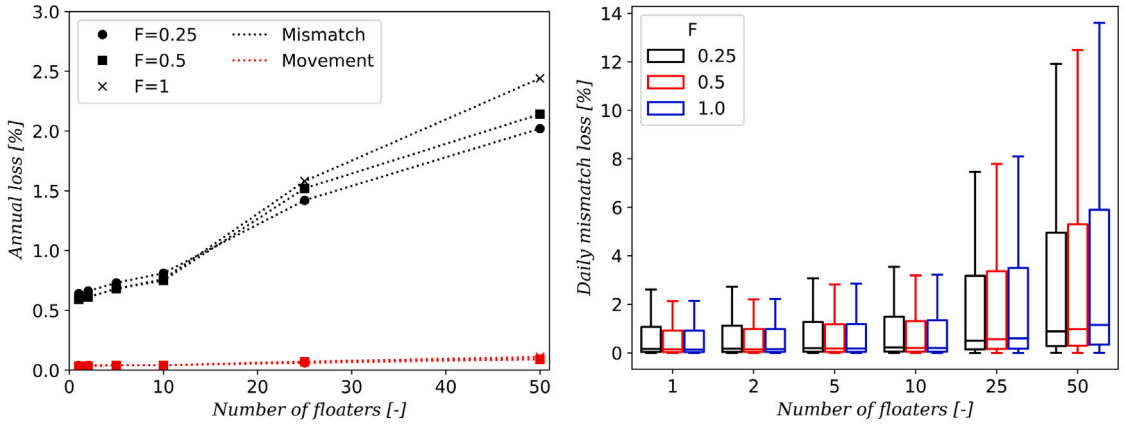

(a) (b)

Fig. 19. (a) Plot of annual power losses and (b) boxplots of the daily mismatch for systems with varying fill factors for an increasing number of floaters.

scenarios showed an elastic dominant response for low floater thickness and a rigid body response for high floater thickness. As a result of this, a thinner floater resulted in lower mismatch losses, due to added resilience from the hydro-elastic response. A similar trend was seen when varying the fill ratio, where a low fill ratio offered lower power mismatch losses due to the hydro-elastic response.

- Based on these observations, a hybrid design approach may be suitable for offshore floating PV platforms. Panels located near the periphery of the platform can be designed to exhibit rigid-body response, thereby reducing structural loads in these floaters. Additionally, the peripheral panels would scatter incoming wave energy, limiting its transmission to the inner regions of the platform. The inner floaters, in turn, could be designed to operate in the elastic regime to minimize motion. This approach offers a balance between structural integrity and energy yield. However, further research is required to determine the optimal configuration for such a hybrid design.

Overall, the manuscript highlights the interplay between the hydro-elastic response and the design and properties of VLFS such as a floating PV platform. The manuscript further presents the consequence of this hydro-elastic response on the potential optoelectric performance of the floating PV platform in offshore conditions.

This manuscript establishes a foundation for progressively exploring additional components of a floating photovoltaic (PV) platform. In our future work, we will include targeted investigations, such as the influence of mooring lines on the structural response and the resulting impact on photovoltaic performance. A three-dimensional analysis will also be undertaken to accommodate irregularly shaped floating PV platforms and various mooring configurations. In addition, the hydro-elastic model will be extended to incorporate non-linearities in both ocean wave dynamics and structural response. The study could also benefit from using the data from irradiance sensors located offshore for increased accuracy. Exploring alternative deployment locations and different types of floating structures, such as membrane-based systems, is also worthwhile. Furthermore, economic factors will be integrated to estimate the levelised cost of energy (LCOE), combining structural and photovoltaic performance with cost analysis to support informed decision-making.

CRediT authorship contribution statement

Alba Alcañiz: Writing – original draft, Visualization, Validation, Software, Methodology, Formal analysis. **Shagun Agarwal:** Writing – original draft, Visualization, Validation, Software, Methodology, Formal analysis. **Philipp Tiwald:** Software, Methodology, Formal analysis. **Olindo Isabella:** Writing – review & editing, Supervision, Funding acquisition. **Hesan Ziar:** Writing – review & editing, Supervision, Methodology, Funding acquisition, Conceptualization. **Oriol Colomés:** Writing – review & editing, Supervision, Methodology, Funding acquisition, Conceptualization.

Declaration of competing interest

The authors declare that they have no known competing financial interests or personal relationships that could have appeared to influence the work reported in this paper.

Acknowledgments

The research leading to these results has received funding from the Horizon 2020 Program, under Grant Agreement 952957, Trust-PV project. S. Agarwal was partially supported by the Dutch Research Council (NWO) grant number OCENW.XS22.1.051.

Data availability

The program used and the numerical data analyzed in this manuscript will be made available via open-source repository SURFdrive.

References

[1] Intergovernmental Panel On Climate Change (Ipcc). Climate change 2021 – The physical science basis: Working group I contribution to the sixth assessment report of the intergovernmental panel on climate change. 1st ed. Cambridge University Press; 2023, http://dx.doi.org/10.1017/9781009157896.

[2] Stevens RJAM, Hobbs BF, Ramos A, Meneveau C. Combining economic and fluid dynamic models to determine the optimal spacing in very large wind farms: Combining economic and fluid dynamic models to determine the optimal spacing in very large wind farms. Wind Energy 2017;20(3):465–77. http://dx.doi.org/10.1002/we.2016.

[3] Golroodbari S, Van Sark W. On the effect of dynamic albedo on performance modelling of offshore floating photovoltaic systems. Sol Energy Adv 2022;2:100016. http://dx.doi.org/10.1016/j.seja.2022.100016.

[4] Chirosca A-M, Rusu L, Bleoju A. Study on wind farms in the North Sea area. Energy Rep 2022;8:162–8. http://dx.doi.org/10.1016/j.egyr.2022.10.244.

[5] Silalahi DF, Blakers A. Global atlas of marine floating solar PV potential. In: Solar, vol. 3, MDPI; 2023, p. 416–33. http://dx.doi.org/10.3390/solar3030023.

[6] Alcañiz A, Monaco N, Isabella O, Ziar H. Offshore floating PV–DC and AC yield analysis considering wave effects. Energy Convers Manage 2024;300:117897. http://dx.doi.org/10.1016/j.enconman.2023.117897.

[7] Trapani K, Millar DL. Floating photovoltaic arrays to power the mining industry: A case study for the McFaulds lake (Ring of Fire). Environ Prog Sustain Energy 2016;35(3):898–905. http://dx.doi.org/10.1002/ep.12275, _eprint: https://aiche.onlinelibrary.wiley.com/doi/pdf/10.1002/ep.12275.

[8] Berstad A, Grøn P. Model basin testing of a floating solar PV plant compared to analysis. In: 10th conference on computational methods in marine engineering. CIMNE; 2023, http://dx.doi.org/10.23967/marine.2023.094.
[9] Golroodbari SZ, Sark W. Simulation of performance differences between offshore and land-based photovoltaic systems. Prog Photovolt, Res Appl 2020;28(9):873–86. http://dx.doi.org/10.1002/pip.3276.
[10] Sree DK, Law AW-K, Pang DSC, Tan ST, Wang CL, Kew JH, et al. Fluid-structural analysis of modular floating solar farms under wave motion. Sol Energy 2022;233:161–81. http://dx.doi.org/10.1016/j.solener.2022.01.017.
[11] Ikhennicheu M, Danglade B, Pascal R, Arramounet V, Trébaol Q, Gorintin F. Analytical method for loads determination on floating solar farms in three typical environments. Sol Energy 2021;219:34–41. http://dx.doi.org/10.1016/j.solener.2020.11.078.
[12] Dörenkämper M, van der Werf D, Sinapis K, de Jong M, Folkerts W. Influence of wave induced movements on the performance of floating PV systems. In: 36th European photovoltaic solar energy conference and exhibition. 2019, p. 1759–62.
[13] Kumar M, Nysted VS, Otnes G, Kjeldstad T, Roosloot N, Selj JH. Impact of water waves on the output power of floating PV systems on water bodies. In: 8th world conference on photovoltaic energy conversion. 2022.
[14] Claus R, López M. Key issues in the design of floating photovoltaic structures for the marine environment. Renew Sustain Energy Rev 2022;164:112502. http://dx.doi.org/10.1016/j.rser.2022.112502.
[15] Colomés O, Verdugo F, Akkerman I. A monolithic finite element formulation for the hydroelastic analysis of very large floating structures. Internat J Numer Methods Engrg 2023;124(3):714–51. http://dx.doi.org/10.1002/nme.7140.
[16] Dean RG, Dalrymple RA. Water wave mechanics for engineers and scientists. In: Advanced series on ocean engineering, World Scientific; 1991.
[17] Bezanson J, Edelman A, Karpinski S, Shah VB. Julia: A fresh approach to numerical computing. SIAM Rev 2017;59(1):65–98. http://dx.doi.org/10.1137/141000671.
[18] Badia S, Verdugo F. Gridap: An extensible finite element toolbox in Julia. J Open Source Softw 2020;5(52):2520. http://dx.doi.org/10.21105/joss.02520.
[19] Verdugo F, Badia S. The software design of Gridap: A finite element package based on the Julia JIT compiler. Comput Phys Comm 2022;276:108341. http://dx.doi.org/10.1016/j.cpc.2022.108341.
[20] Colomes Gene O. Code used to generate the data underlying the publication: A monolithic Finite Element formulation for the hydroelastic analysis of Very Large Floating Structures. 4TU.ResearchData; 2022, http://dx.doi.org/10.4121/19601419.
[21] Khabakhpasheva T, Korobkin A. Hydroelastic behaviour of compound floating plate in waves. J Engrg Math 2002;44(1):21–40. http://dx.doi.org/10.1023/A:1020592414338.
[22] Liu X, Wang X, Xu S. A DMM-EMM-RSM hybrid technique on two-dimensional frequency-domain hydroelasticity of floating structures over variable bathymetry. Ocean Eng 2020;201:107135. http://dx.doi.org/10.1016/j.oceaneng.2020.107135.
[23] Yago K, Endo H. On the hydoroelastic response of box-shaped floating structure with shallow draft. J Soc Nav Archit Jpn 1996;1996(180):341–52. http://dx.doi.org/10.2534/jjasnaoe1968.1996.180_341.
[24] KNMI. API developer portal. 2023, URL https://developer.dataplatform.knmi.nl/apis.
[25] KNMI. KNW-CSV-TS-UPDATE. 2023, URL https://dataplatform.knmi.nl/dataset/knw-csv-ts-update-1-0.
[26] Yu Y, Pei H, Xu C. Parameter identification of JONSWAP spectrum acquired by airborne LIDAR. J Ocean Univ China 2017;16(6):998–1002. http://dx.doi.org/10.1007/s11802-017-3271-2, URL http://link.springer.com/10.1007/s11802-017-3271-2.
[27] Hasselmann K, Barnett TP, Bouws E, Carlson H, Cartwright DE, Enke K, et al. Measurements of wind-wave growth and swell decay during the joint north sea wave project (JONSWAP). Ergaenzungsheft Zur Dtsch Hydrogr Z Reihe A 1973.
[28] Perez R, Seals R, Ineichen P, Stewart R, Menicucci D. A new simplified version of the perez diffuse irradiance model for tilted surfaces. Sol Energy 1987;39(3):221–31. http://dx.doi.org/10.1016/S0038-092X(87)80031-2.
[29] F. Holmgren W, W. Hansen C, A. Mikofski M. pvlib python: a python package for modeling solar energy systems. J Open Source Softw 2018;3(29):884. http://dx.doi.org/10.21105/joss.00884.
[30] Micheli L. The temperature of floating photovoltaics: Case studies, models and recent findings. Sol Energy 2022;242:234–45.
[31] Liu H, Krishna V, Lun Leung J, Reindl T, Zhao L. Field experience and performance analysis of floating PV technologies in the tropics. Prog Photovolt, Res Appl 2018;26(12):957–67.
[32] Majumder A, Innamorati R, Frattolillo A, Kumar A, Gatto G. Performance analysis of a floating photovoltaic system and estimation of the evaporation losses reduction. Energies 2021;14(24):8336.
[33] Goswami A, Sadhu P, Goswami U, Sadhu PK. Floating solar power plant for sustainable development: A techno-economic analysis. Environ Prog Sustain Energy 2019;38(6):e13268.
[34] PVsyst SA. PVsyst - Photovoltaic software. 2023, https://www.pvsyst.com/. [Accessed: 23 October 2023].
[35] Faiman D. Assessing the outdoor operating temperature of photovoltaic modules. Prog Photovolt, Res Appl 2008;16(4):307–15.
[36] Dörenkämper M, Wahed A, Kumar A, de Jong M, Kroon J, Reindl T. The cooling effect of floating PV in two different climate zones: A comparison of field test data from the Netherlands and Singapore. Sol Energy 2021;219:15–23.
[37] Smets AHM, Jäger K, Isabella O, Swaaij Rv, Zeman M. Solar energy: The physics and engineering of photovoltaic conversion, technologies and systems. UIT Cambridge; 2016.
[38] Pelaez SA, Deline C, Greenberg P, Stein JS, Kostuk RK. Model and validation of single-axis tracking with bifacial PV. IEEE J Photovoltaics 2019;9(3):715–21.
[39] de Moura ES, Marques HSA, Riffel DB. Assessment of photovoltaic I–V curve translation methods in real-world situations. Sol Energy 2024;276:112654.
[40] Stankov B, Terziev A, Vassilev M, Ivanov M. Influence of wind and rainfall on the performance of a photovoltaic module in a dusty environment. Energies 2024;17(14):3394.
[41] BosswerkGmbH. GreenAkku. 2023, URL https://greenakku.de/Solarmodule/Flexible-Solarmodule/Bosswerk-Sphere-Hoch-Flexibles-Solarmodul-ETFE-200Wp::4499.html.
[42] KNMI. Actuele10mindataKNMIstations. 2023, URL https://dataplatform.knmi.nl/dataset/actuele10mindataknmistations-2.
[43] Boland J, Huang J, Ridley B. Decomposing global solar radiation into its direct and diffuse components. Renew Sustain Energy Rev 2013;28:749–56. http://dx.doi.org/10.1016/j.rser.2013.08.023.
[44] Zhang M, Schreier S. Review of wave interaction with continuous flexible floating structures. Ocean Eng 2022;264:112404. http://dx.doi.org/10.1016/j.oceaneng.2022.112404.
[45] Suzuki H, Riggs HR, Fujikubo M, Shugar TA, Seto H, Yasuzawa Y, et al. Very large floating structures. In: Volume 2: structures, safety and reliability; petroleum technology symposium. San Diego, California, USA: ASMEDC; 2007, p. 597–608. http://dx.doi.org/10.1115/OMAE2007-29758.
[46] Loukogeorgaki E, Michailides C, Angelides DC. Hydroelastic analysis of a flexible mat-shaped floating breakwater under oblique wave action. J Fluids Struct 2012;31:103–24. http://dx.doi.org/10.1016/j.jfluidstructs.2012.02.011.
[47] Agarwal S, Colomés O, Metrikine A. Dynamic analysis of viscoelastic floating membranes using monolithic Finite Element method. 2023, http://dx.doi.org/10.2139/ssrn.4689746.
[48] Jacobson MZ, Jadhav V. World estimates of PV optimal tilt angles and ratios of sunlight incident upon tilted and tracked PV panels relative to horizontal panels. Sol Energy 2018;169:55–66.